Charles University in Prague
Faculty of Science

Ph.D. program: Modelling of Chemical Properties of Nano- and Biostructures

M.Sc. Junjie He

Theoretical Modeling of Two-dimensional Magnetic Materials

Teoretické studium dvojrozměrných magnetických materiálů

Ph.D. Dissertation

Supervisor: Prof. RNDr. Petr Nachtigall, Ph.D.

Prague, 2017

Declaration of Authorship

I, Junjie He, declare that this dissertation titled, " **Theoretical Modeling of Two-dimensional Magnetic Materials**" and the work presented in it is my own. All the literature is properly cited, and I have not been yet awarded any other academic degree or diploma for this thesis or its substantial part.

Signed: _____

Date: _____

Prohlášení:
Prohlašuji, že jsem závěrečnou práci zpracoval/a samostatně a že jsem uvedl/a všechny použité informační zdroje a literaturu. Tato práce ani její podstatná část nebyla předložena k získání jiného nebo stejného akademického titulu.

V Praze,

Podpis

I dedicate this thesis to

my wife, Ling, my beloved son, Xuanzhu and my cat, Benben

for their uncondictional support and love.

Acknowledgment

First of all, I would like to express my sincere gratitude to my supervisor, Prof. Petr Nachtigall, for giving me an opportunity to work, study and live in Prague. I have three years of pleasant time in here, which is a part of most precious memory in my life. I deeply appreciated his great encouragement, nice guidance, and warm assistance through the years in my research and life. This thesis would not have been possible without his supports and efforts.

Second, my sincere thanks go to Dr. Ota Bludský in IOCB of Czech Academy of Sciences for providing me a part-time research position in his team, which makes my Ph.D. research productive. Next, I am grateful to my colleagues, M.Sc. Miroslav Položij, M. Sc. Pengbo Lyu, Dr. Viet Thang Ho, Dr. Ángel Morales-García, Dr. Miroslav Rubeš and Dr. Lukáš Grajciar for their insightful discussions, for their help in life and work, for all the fun we have had in the last three years. I also would like to thank Prof. Michael J. Bojdys in CUNI, Dr. Xiao Li in UT Austin, Dr. Shuangying Ma in Stuttgart and my master‘s advisor Prof. Lizhong Sun in XTU for their wonderful collaboration.

Finally, I would like to thank my wife, Ling, my son, Xuanzhu, my cat, Benben and all my family members for providing me with constant support and continuous encouragement throughout Ph.D. study. Thank you!

Junjie He

In Prague

July 2017

Abstract

Two dimensional (2D) materials, such as graphene, phosphorene and transition metal chalcogenides, have received a great attention in recent years due to their unique physical and chemical properties. A majority of 2D materials is intrinsically non-magnetic, therefore, their applications in spintronics are limited. The design and synthesis of new 2D materials with intrinsic magnetism and high spin-polarization remains a challenge.

Computational discovery of new 2D materials with desired magnetic and electronic properties is the subject of this thesis. Using density functional theory with PBE, PBE+U and HSE06 functionals, we have systematically investigated the structure, electronic, magnetic and topological properties of novel 2D materials. Investigated materials include MXenes and layered transition-metal trihalides, both with great potential applications in spintronic devices. Four different classes of materials showing unique magnetic properties were investigated and reported in this thesis.

(1) Asymmetrically functionalized MXenes were studied. The coexistence of the fully compensated antiferromagnetic order (zero magnetization) and completely spin-polarized semiconductivity was found for the first time. Moreover, the spin carrier orientation and induced transition from bipolar antiferromagnetic semiconductors to half-metal antiferromagnets can be easily controlled by using an electron or hole doping. The spin-polarized semiconductivity with zero magnetism is also preserved when MXenes are put on the SiC(0001) support.

(2) The electronic and magnetic properties of new two-dimensional Mn-based MXenes (Mn_2CT_2, T = F, Cl, OH, O, and H) were investigated. The results showed that these materials are intrinsic half-metals with high Curie temperature (520 K), wide half-metallic gap (0.9 eV) and a sizable magnetic anisotropy (24 μeV). These magnetic properties make the Mn_2CF_2 MXene an optimal material for applications in spintronics. Different surface functional groups lead to either quantitative (Cl and OH) or qualitative (O and H) changes of Mn_2CT_2 magnetic properties. It is proposed that Mn_2CT_2 MXenes can be prepared experimentally from already existing parent Mn_2GaC MAX phase by exfoliation techniques.

(3) The structural stability and electronic and magnetic properties of VCl_3 and VI_3 crystals were systematically investigated. Both VCl_3 and VI_3 had intrinsic ferromagnetism and half-metallicity with rather rare single spin Dirac point. Contrary to the Dirac point in graphene, the Dirac points in VCl_3 and VI_3 monolayers are mainly due to the V-*d* electrons and

consequently they show large spin-orbital coupling-induced gaps of about 29 and 12 meV for VCl_3 and VI_3 monolayers, respectively. Calculated small cleavage energies indicates the feasibility of an exfoliation from VCl_3 and VI_3 layered bulk phases. Our results greatly broadened the family of potential 2D Dirac materials, opening the way towards the development of high-performance electronic devices.

(4) The electronics, magnetic and topological insulator properties of NiCl3 monolayer were studied. $NiCl_3$ monolayer was found to be a new class of Dirac materials with Dirac spin-gapless semiconducting properties and high-temperature ferromagnetism. Moreover, taking into account the spin-orbit coupling, the $NiCl_3$ monolayer becomes an intrinsic Chern insulator with a large non-trivial band gap of ~24 meV, corresponding to an operating temperature as high as ~280 K at which the quantum anomalous Hall (QAH) effect could be observed. The novel transport properties for QAH effect have been confirmed by the topological edge states calculations.

Souhrn

Vzhledem ke svým jedinečným chemickým a fyzikálním vlastnostem se dvojrozměrné (2D) materiály odvozené od grephenu, phosporenu či chalkogenidů tranzitních kovů těší velkému zájmu chemiků a fyziků. Drtivá většina těchto 2D materiálů není magnetická a jejich potenciální využití ve spintronice není přímočaré. Návrh a příprava nových 2D materiálů vykazujících magnetické vlastnosti a vysokou spinovou polarizovatelnost zůstává aktuální výzvou.

Předmětem této dizertační práce je hledání 2D materiálů s požadovanými magnetickými a elektrickými vlastnostmi pomocí počítačových studií. Struktura, elektronické, magnetické a topologické vlastnosti nových 2D materiálů byly systematicky studovány pomocí metod funkcionálu hustoty s využitím PBE, PBE+U a HSE06 funkcionálů. Mezi studované systémy patří materiály odvozené od MXenů a vrstevnatých trihalidů tranzitních kovů. U obou typů systémů byly předpovězeny jedinečné magnetické a elektrické vlastnosti, ze kterých je patrný jejich obrovský potenciál pro aplikace ve spintronice.
Dizertační práce popisuje vlastnosti celkem čtyř nově navržených materiálů s ojedinělými magnetickými vlastnostmi:

(1)Asymetricky funkcionalizované MXeny. MXeny jsou 2D materiály sestávající z tranzitního kovu a uhlíku (nebo dusíku). Bylo zjištěno, že asymetricky funkcionalizované MXenů (na horní a dolní povrch MXenu je navázána jiná funkční skupina) vykazují jednak plně kompenzované antiferomagnetické uspořádání elektronů a jednak spinově závislé polovodičové charakteristiky. Dále bylo zjištěno, že charakter spinově závislého polovodiče může být kontrolován pomocí vloženého napětí a může tak změnit bipolární antiferomagnetický polovodič na tzv. half-metallic polovodič. Magnetické vlastnosti MXenů nejsou ovlivněny interakcí s SiC nosičem.

(2) 2D manganový MXen. Byly studovány elektronické a magnetické vlastnosti Mn_2CT_2 MXenů (T = F, Cl, OH, O a H). Bylo zjištěno, že tyto materiály jsout tzv. half-metals s vysokou Curieovou teplotou (520 K pro Mn_2CF_2), šikorkým half-matellic pásem (0.9 eV) a značnou magnetickou anizotropií (24 μeV). Různé funkční skupiny na povrchu Mn_2C vedou buďto ke kvantitativní změně vlastností (Cl a OH) nebo ke kvalitativním změnám magnetických vlastností (O a H). Na základě výpočtů (exfoliačních energií) lze předpokládat, že tyto materiály je možné připravit z již existující 3D Mn_2GaC MAX fáze.

(3) VCl_3 a VI_3 lamely. Systematicky byly studovány strukturní, elektronické a magnetické vlastnosti VCl_3 a VI_3 2D materiálů. Oba vykazují ferromagnetizmus a tzv. half-metallic charakter a zejména vykazují Diracův bod pouze pro jeden spin. Na rozdíl od materiálů odvozených od graphenu je Diracův bod v námi studovaných materiálech způsoben dominantně *d*-elektrony kovu a tudíž vykazují široký pás způsobený silnou spin-orbitální interakcí (29 meV pro VCl_3 a 12 meV pro VI_3). Vypočtená malá exfoliační energie indikuje možnost přípravy těchto 2D materiálů.

(4) Monovrstva $NiCl_3$. Byly studovány magnetické a topologické vlastnosti $NiCl_3$ monovrstev. Bylo zjištěno, že se jedná o novou třídu Diracova materiálu charakterizovanou tzv. spin-gapless polovodivostí a vysokoteplotním ferromagnetizmem. Zahrnutí spin-orbitální interakce vede k tzv. Chernovo izolátoru s vysokým netriviálním rozdílem mezi pásy (24 meV). Tomu odpovídá teplota 280 K, za které by mohl být pozorován kvantový anomální Hallův efekt. Toto zjištění bylo dále potvrzeno existencí topologických hraničních („edge“) stavů.

Zde prezentovaná studie ukazuje mimořádné magnetické vlastnosti několika nově navržených 2D materiálů. Pokud se tyto materiály podaří experimentálně připravit a vhodně manipulovat, daly by se úspěšně využít při konstrukci elektronických zařízení nové generace.

Contents

List of Figures

List of Tables

Abbreviations

DFT	**D**ensity **F**unction **T**heory
DFT+U	**D**ensity **F**unction **T**heory Plus Hubbard **U**
LDA	**L**ocal **D**ensity **A**pproximation
GGA	**G**eneralized **G**radient **A**pproximation
PBE	**P**erdew-**B**urke-**E**rnzerhof
HSE	**H**eyd-**S**cuseria-**E**rnzerhof
SGS	**S**pin **G**apless **S**emiconductor
BMS	**B**ipolar **M**agnetic **S**emiconductor
HM	**H**alf-**m**etal
AIMD	***a**b **i**nitio* **M**olecular **D**ynamics
FM	**F**erro**m**agnetism
AFM	**A**nti**f**erro**m**agnetism
VBM	**V**alence **B**and **M**aximum
CBM	**C**onduction **B**and **M**inimum
MAE	**M**agnetic **A**nisotropy **E**nergy
SOC	**S**pin **O**rbital **C**oupling
QAH	**Q**uantum **A**nomalous **H**all
MXenes	Two-dimensional Transition-metal Carbide/Nitrite
TMT	**T**ransition **M**etal **T**rhalides
TM	**T**ransition-**M**etal

Chapter 1 Introduction

Spintronics (from spin transport electronics) consider intrinsic spin of the electron and its associated magnetic moment.[1,2] It is one of the most promising field of technology, in particular for speeding up data processing and transmission with lower energy consumption in high-performance electronic devices. The great challenge for practical applications of spintronics is the lack of the suitable materials with high spin-polarization, room-temperature magnetic order and high carrier mobility. Spintronics materials can be classified as half-metals (HM), spin-gapless semiconductors (SGS) and bipolar magnetic semiconductors (BMS) (Figure 1). Half-metals exhibit metallic behavior in one spin channel they behave as an insulator or a semiconductor in the opposite spin channel as shown in Figure 1a. Half-metals with 100% spin-polarization can be used as spin filters in electronic devices.[3] Spin gapless semiconductors have a zero gap just in one spin channel (Figure 1b), conducting spin-polarized electrons and holes in this materials.[4] There is no threshold energy required to excite electrons from the valence band to the conduction band (zero band gap). Some remarkable properties have been observed experimentally in SGS such as a vanishing Seebeck coefficient, a nearly temperature-independent conductivity, and a giant magnetoresistance effect.[5] The bipolar magnetic semiconductors (BMS) show the semiconductor characteristics with opposite spin-polarized directions between the valence band and the conduction band, as shown in Figure 1c. The reversible spin-polarization in BMS can be controlled by a gate voltage, which makes these materials suitable for the generation and manipulation of spin currents in spintronic devices.[6,7] However, the most of spintronics properties have been found and predicted for bulk materials. The reduction in the size of devices requires the low-dimensional materials for the spin-based nanoscale device.

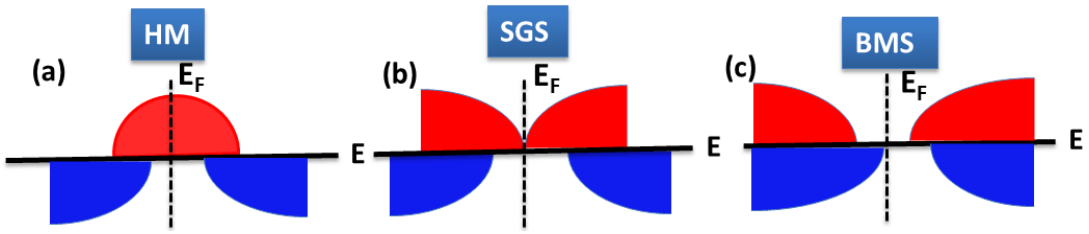

Figure 1. 1 Schematic plot of electronic structures for various spintronics materials: (a) HM, (b) SGS, (c) BMS.

Inspired by the discovery of graphene by Geim and Novoselov in 2004,[8,9]two dimensional materials obtained an enormous attention due to its unique physical and chemical properties required for the next-generation of electronic and spintronic devices.[10,11] Particularly, 2D Dirac materials exhibit novel physical properties such as linear band dispersion, enormously high carrier mobility, and topological phases.[12,13,14] However, a majority of 2D materials are intrinsically non-magnetic, consequently their applications in spintronics are widely limited. Although the doping, defects, absorption and functionalization in various 2D materials can induce high spin-polarization, half-metallic character and magnetic effects, it remains a challenge for experiment to prepare materials with an ordered spin structure and high spin-polarization at room temperature.[15,16,17] Dopant or defect distributions in 2D materials cannot be easily controlled in experiment and the dopant clustering effects represent additional complications.[18] The nanoribbons of 2D materials (graphene in particular) can be turned into a HM material by external electric field.[19] Unfortunately, the requirement of strong external electric field inevitably limits its practical application. Therefore, the development of new materials with intrinsic ferromagnetism and spin-polarization is of a great importance for both a fundamental interest and applications in spintronics.

The MAX phase has a general formula $M_{n+1}AX_n$ and it consists of $M_{n+1}X_n$ blocks separated by A-layers (M is transition metal, A is an A-group element and X is either carbon or nitrogen). MXenes were prepared experimentally from the corresponding MAX phase by exfoliation in hydrofluoric acid.[20,21,22] The synthesized MXenes are generally terminated with a surface element/group such as H, F, and OH. The MXenes have attracted great attention due to their potential applications in sensors, catalysis, energy storage and nanoelectronics.[21,22] Previous investigations haves demonstrated that Ti, Ta and Cr based MXenes have magnetic properties.[23,24,25,26] However, the magnetism of MXenes generally disappears when their surfaces are functionalized due to the completely compensated antiferromagnetic (AFM) ground states. For example, theoretical investigations have confirmed that Cr_2CT_2 (T = OH, H, F and Cl), Ti_2CO_2, and V_2CT_2 (T = F, OH) are AFM semiconductors or metals.[27,28,29] Although the bare Cr_2C is predicted to be ferromagnetic (FM) half-metal, experimentally prepared MXenes have always surfaces terminated with F, OH or other atoms. The functionalized MXenes are thermodynamically more stable than the unfunctionalized ones. Therefore, it is very important to investigate the spin-polarization and magnetic property for new MXenes materials for potential spintronics application. In Section 3.1 we propose a new type of spintronics materials, with coexistence of antiferromagnetism

and spin-polarized semiconductivity, obtained simply by an asymmetrical functionalization of Cr_2C sheet. In section 3.2, we report the electronic and magnetic properties of new Mn-based MXenes, which can be prepared experimentally from the already existing parent Mn_2GaC MAX phase by exfoliation techniques. Transition metal trhalides (TMT), a family of layered materials with the general formula TMX_3 (X=Cl, Br, I) have unique structure and unique electronic and magnetic properties.[30,31,32] The TMT materials have TM centers in an octahedral environment with a TM honeycomb arrangement. Such van der Waals materials stacked on top of each other can be exfoliated into 2D materials from the bulk phase, as has been shown experimentally, e.g., for TM chalcogenides and graphite.[33] Indeed, the $RuCl_3$, $CrCl_3$, CrI_3 bulk phases have been exfoliated into monolayer (or few-layers) recently.[34,35,36,37] In particular, the 2D ferromagnetism in monolayer CrI_3 has been confirmed experimentally with an intriguing thickness-dependent magnetic phase transition.[36] Interestingly, the van der Waals heterostructures of CrI_3 and WSe_2 also have been prepared experimentally.[38] Such hybrid ferromagnet/semiconductor materials show the sizable spin and valley pseudospin properties for promising spintronics and valleytronics applications. Moreover, the $RuCl_3$ was found to be the spin-orbit coupled Mott insulator with a possible Kitaev quantum spin liquid states, thus offering promising applications in the development of future topological quantum bits.[34] However, the electronic and magnetic properties in this type of materials have not been completely understood yet. We report the Dirac half-metallic and Dirac gapless semiconducting properties of VCl_3 and $NiCl_3$ monolayers in sections 3.3 and 3.4. Particularly, the $NiCl_3$ is found to be a magnetic topological insulator (Chern insulator) with a large non-trivial gap and high-temperature ferromagnetism, which makes it an excellent candidate for the realization of the QAH effect.

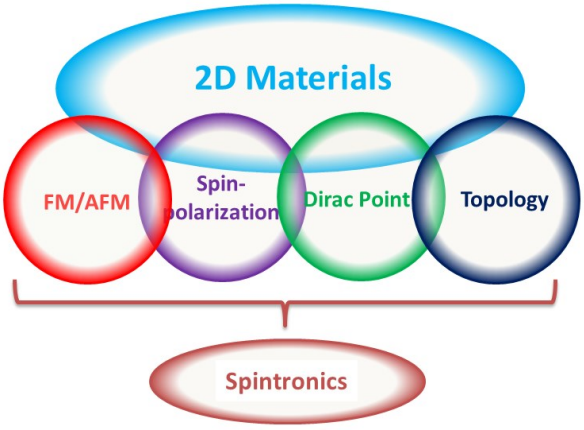

Figure 1. 2 Schematic plots with different spintronics materials.

We have focused our investigation reported in this thesis on new 2D materials. We were interested in understanding of various magnetic properties important for next-generation electronic devices. It includes Dirac point, intrinsic magnetic order (ferromagnetism (FM) and antiferromagnetism (AFM)), as well as the topological properties (Figure 1.2). Results reported in section 3 shows that we were able to predict theoretically desired properties for several materials. It remains to be seen if these materials are experimentally achievable.

Charpter 2 Methods

2.1 DFT methods

The Density functional theory (DFT) is the most successful computational method to investigate the electronic structure of atoms, molecules, and condensed phase matter. The many body Hamitonion (H) including all interaction terms for M nuclei and N electrons can be written as:

$$H = -\frac{1}{2}\sum_{i}^{N}\nabla_i^2 - \frac{1}{2}\sum_{A=1}^{M}\frac{1}{M_A}\nabla_A^2 - \sum_{i=1}^{N}\sum_{A=1}^{M}\frac{Z_A}{r_{iA}} + \sum_{i=1}^{N}\sum_{i\neq j}^{N}\frac{1}{r_{ij}} + \sum_{A=1}^{M}\sum_{A\neq B}^{M}\frac{Z_A Z_B}{r_{AB}}, \tag{2.1}$$

Here, A and B sum over the M nuclei while i and j denote the N electrons in the system. The first two terms describe the kinetic energy of the electrons and nuclei, respectively. The remaining three terms represent the the electrostatic interactions between the nuclei and the electrons, the electron-electron Coulomb repulsion and nucleus-nucleus interactions, respectively. The motion of nuclei and electrons can be separated, which is called Born-Oppenheimer approximation.[39] The many body system can be simplified to only considere electronic Schrödinger equation:

$$H_{elec}\Psi_{elec} = E\Psi_{elec}, \tag{2.2}$$

where the so-called electronic Hamiltonian can be expressed as

$$H_{elec} = -\frac{1}{2}\sum_{i}^{N}\nabla_i^2 - \sum_{i=1}^{N}\sum_{A=1}^{M}\frac{Z_A}{r_{iA}} + \sum_{i=1}^{N}\sum_{i\neq j}^{N}\frac{1}{r_{ij}} = T + E_{ne} + E_{ee}. \tag{2.3}$$

While conventional quantum chemical methods are based on the wavefunction formalism, DFT uses the electron density as the central quality. Hohenberg and Kohn proved that the ground-state energy of the system is uniquely determined by the ground-state electron density.[40] The ground-state electronic energy is a functional of electronic density. The electron density $\rho(\vec{r})$ can be defined as the following multiple integral over the spin coordinates of all electrons and over all but one of the spatial variables:

$$\rho(\vec{r}) = N\int\ldots\int\left|\Psi(\vec{x}_1,\vec{x}_2,\ldots,\vec{x}_N)\right|^2 ds_1 d\vec{x}_2\ldots d\vec{x}_N, \tag{2.4}$$

The energy expressed as a functional of electron density can be written as:

$$E[\vec{\rho}] = T[\vec{\rho}] + E_{ne}[\vec{\rho}] + E_{ee}[\vec{\rho}], \tag{2.5}$$

The exact functional exprissions for $T[\vec{\rho}]$ and $E_{ee}[\vec{\rho}]$ are yet unknown, which is a main challenge in DFT methods. The Kohn-Sham proposed that the kinetic term $T[\vec{\rho}]$ can be approximated by using reference system of non-interacting electrons. The kinetic energy term can then be expressed as:

$$T[\vec{\rho}] = T_{ni}[\vec{\rho}] + T_c[\vec{\rho}] = -\frac{1}{2}\sum_{i}^{N}\langle\varphi_i|\nabla^2|\varphi_i\rangle + T_c[\vec{\rho}], \tag{2.6}$$

$T_{ni}[\vec{\rho}]$ and φ_i represent the kinetic energy of non-interacting electrons and Kohn-Sham orbitals, respectively. $T_c[\vec{\rho}]$ is the kinetic correlation energy, which represent the deviation between real kinetic energy and kinetic energy of reference system (non-interacting electrons). The $E_{ee}[\vec{\rho}]$ can be expressed as

$$E_{ee}[\vec{\rho}] = J[\vec{\rho}] + \Delta E_{ee}[\vec{\rho}] = \frac{1}{2}\iint\frac{\rho(\vec{r}_1)\rho(\vec{r}_2)}{r_{12}}d\vec{r}_1 d\vec{r}_2 + \Delta E_{ee}[\vec{\rho}], \tag{2.7}$$

where $J[\vec{\rho}]$ is a classical coulomb repulsion energy and $\Delta E_{ee}[\vec{\rho}]$ represents a deviation of the real electron–electron interaction energy from a classical coulomb repulsion energy and this term contains the electron exchange, electron correlation and self-interaction contributions. Unknown parts of kinetic term and electron-electron interactions is called exchane-correlation functional and it is defined as[41]

$$E_{xc}[\vec{\rho}] = \Delta E_{ee}[\vec{\rho}] + T_c[\vec{\rho}]. \tag{2.8}$$

It follows that the Kohn-Sham energy expression can be written as follows:

$$\begin{aligned} E[\vec{\rho}] &= T_{ni}[\vec{\rho}] + E_{ne}[\vec{\rho}] + J[\vec{\rho}] + E_{xc}[\vec{\rho}] \\ &= -\frac{1}{2}\sum_{i}^{N}\langle\varphi_i|\nabla^2|\varphi_i\rangle + \int V_{ne}\rho(\vec{r})d\vec{r} + \frac{1}{2}\iint\frac{\rho(\vec{r}_1)\rho(\vec{r}_2)}{r_{12}}d\vec{r}_1 d\vec{r}_2 + E_{xc}[\vec{\rho}] \end{aligned}. \tag{2.9}$$

Only the last term – the exact expression for exchange-correlation functional – remains unknown. The ground-states energy can be obtained by solving the Kohn-Sham equations in self-consistent manner:[41]

$$h^{KS}\varphi_i = (\frac{1}{2}\nabla^2 + V_{ne} + \frac{1}{2}\int\frac{\rho(\vec{r}_2)}{r_{12}}d\vec{r}_2 + V_{xc})\varphi_i = \varepsilon_i\varphi_i, \tag{2.10}$$

The h^{KS} and V_{xc} is a one-electron Kohn-Sham operator and exchange correlation potential, respectively. In principle, the Kohn-Sham functional of energy expression is an exact. The main challenge is that we do not know the exact form of exchange-correlation functional.

The local density approximation (LDA) is the simplest approximation for the exchange-correlation energy, which can be written in a simple form: [42]

$$E_{xc}^{LDA}[\rho] = \int \rho(\vec{r})\varepsilon_{xc}(\rho(\vec{r}))d\vec{r}\,, \tag{2.11}$$

where ε_{xc} is the exchange-correlation energy per particle of a uniform electron gas of density ρ(r). LDA is based on the uniform electron gas model[43,44,45], which works reasonably well for relatively constatnt densities but it starts to fail for systems with large density gradient. To improve the description of the correlation energy is to add the effects of the density gradient within the scheme of generalized-gradient approximation (GGA).[46,47]

$$E_{xc}^{GGA}[\rho] = \int \rho(\vec{r})\varepsilon_{xc}(\rho(\vec{r}),\nabla\rho(\vec{r}))d\vec{r}\,, \tag{2.12}$$

The most widely used GGAs are the forms proposed by Perdew, Burke and Enzerhof (PBE).[48] The PBE can provide resonable results in solid states calculations in particular. However, the PBE level generally underestimates the band gap compared to the experimental value. This shortcoming can be overcome either by the DFT+U approach (see next subsection) or with the hybrid functionals. The exchange-correlation functional in the latter approach incorporates a mixture of exact Hatree-Fock exchange term using Kohn-Sham orbitals:

$$E_x^{HF} = -\sum_i^n \sum_j^n \left\langle \varphi_i^{KS}(1)\varphi_j^{KS}(2)\left|\frac{1}{r_{ij}}\right|\varphi_i^{KS}(2)\varphi_j^{KS}(1)\right\rangle, \tag{2.13}$$

The greneral form for hybrid-functional can be written as follows:

$$E_{xc}^{hybrid} = E_{xc}^{GGA} + \lambda E_x^{HF}\,. \tag{2.14}$$

The most commonly used hybrid functionals are B3LYP[49,50], HSE[51] and PBE0[52]. The HSE functional was mainly used in this work to correct the band gap of PBE calculations, which have been widely applied in the calculations of electronic and optical properties of two-dimensional materials.

2.3 The DFT+U and linear-response theory

The GGA fails to describe the localization of *d* or *f* electrons in transition-metal compounds. The GGA+U method[53] is an approximation which corrects GGA in order to better describe the strongly correlated systems. A successful example is Cu-based superconductor $CaCuO_2$ and La_2CuO_4.[53] The DFT+U approach can give the correct antiferromagnetic insulating ground-state for Cu-based superconductors instead of predicting non-magnetic metal as obtained from LDA and GGA levels (due to underestimate exchange splitting between spin-up and spin-down electrons). The rotationally invariant DFT+U formalism proposed by

Dudarev et al.[54] is used in thisthesis, where only the effective Coulomb interaction $U_{eff} = U - J$ value is meaningful instead of individual U and J values.

In the Dudarev approach, the energy functional can be writen as follows:[54]

$$E_{DFT+U} = E_{DFT} + E_U \,, \tag{2.15}$$

where the effective on-site Coulomb interaction E_U has the following form:[54]

$$E_U = \frac{U}{2}\sum_I \sum_{m,\sigma} n^{I\sigma}_{mm} - \sum_I n^{I\sigma}_{mm'} n^{I\sigma}_{m'm} = \frac{U}{2}\sum_{I,\sigma} Tr[n^{I\sigma}(1-n^{I\sigma})] \,, \tag{2.16}$$

where $n^{I\sigma}_{mm'}$ is a generalized atomic orbital occupation for the atom at site I and spin σ.

The appropriate U parameter for transition-metal ions in real materials strongly depends on its chemical environment, which is usually obtained by fitting the experimental observation. Cococcioni et al.[55] proposed that the effective U parameter can be evaluated by a linear response theory (LRT). In this method, by applying a local perturbation α to local orbital, the change of occupations can be induced. The interacting χ_{IJ} and non-interesting χ^0_{IJ} response function can be defined with respect to the perturbation α :

$$\chi_{IJ} = \frac{\partial^2 E}{\partial \alpha_I \partial \alpha_J} = \frac{\partial n_I}{\partial \alpha_J} \,, \tag{2.17}$$

$$\text{and } \chi^0_{IJ} = \frac{\partial^2 E^0}{\partial \alpha^0_I \partial \alpha^0_J} = \frac{\partial n_I}{\partial \alpha^0_J} \,, \tag{2.18}$$

The effective Hubbard U_{eff} is calculated from the difference between inverse of the response matrix χ_{IJ} and χ^0_{IJ} :

$$U_{eff} = (\chi^0_{IJ})^{-1} - (\chi_{IJ})^{-1} \,. \tag{2.19}$$

The linear-response Hubbard U approach have been successfully applied to predict the ground state of the (Mg,Fe)(Si,Fe)O_3 perovskites with high-spin Fe atoms and a pressure-induced spin-state crossover for Fe atoms and the results were consistent with the x-ray diffraction and Mossbauer spectroscopy measurements.[56] The linear-response Hubbard U theory combined with the hybrid functional (HSE06) was used to investigated the electronic and magnetic properties of 2D materials in this thesis.

2.4 Lattice dynamics and phonons

To calculate the lattice dynamical properties of two-dimensional materials, the density functional perturbation theory (DFPT) have been widely applied,[57] and it is implementd in Quantum Expresso[58] and Phonopy packages[59,60]. A perturbation applied to an atom, a small displacements from the equilibrium position of atom is used. Detailed expressions can be found in Ref.[57,61]. Phonon spectrum can be calculated by the dynamical matrix

$$D_{ij}(\vec{q}) = \sum_{\vec{R}} e^{-i\vec{q}.\vec{R}'} \frac{\partial^2 E}{\partial u_i(\vec{R}+\vec{R}')\partial u_j(\vec{R})}, \tag{2.20}$$

with respect to the atomic displacements $u(\vec{R})$ for each atom in each direction (i and j correspond to x, y and z coordinates) by solving the matrix equation

$$D_{ij}(\vec{q})\vec{\varepsilon} = M\omega_{\vec{q}}^2\vec{\varepsilon}\,, \tag{2.21}$$

which gives the phonon frequencies $\omega_{\vec{q}}$ of the phonons with wave vector $\vec{q}$. The phonon spectrum is important for an investigation of the dynamics of two-dimensional materials. The knowledge of the phonon spectrum is essential for understanding the dynamic stability of 2D materials.

2.5 *Ab initio* molecular dynamics

The potential energy of nuclei is explicitly evaluated at the DFT level in *ab initio* molecular dynamics. Within the concept of the Born-Oppenheimer molecular dynamic (BOMD), the potential energy $E[\{\phi_i\};\boldsymbol{R}]$ is minimized at every MD step with respect to Kohn-Sham orbitals $\{\phi_i(\boldsymbol{r})\}$ under the orthonormalization constraint $\langle\phi_i(\boldsymbol{r})|\phi_j(\boldsymbol{r})\rangle = \sigma_{ij}$. This leads to the following Lagrangian:[62]

$$L_{BO}(\{\phi_i\};\boldsymbol{R},\dot{\boldsymbol{R}} \quad \angle \overline{I=1} \quad \dot{\boldsymbol{R}} \quad \{\varphi_i\} \quad \_ \ \ i\};\boldsymbol{R}] + \sum_{i,j}\Lambda_{ij}(\langle\varphi_i|\varphi_j\rangle - \delta_{ij}), \tag{2.22}$$

where Λ is the Lagrangian multiplier matrix. Solving the Euler-Lagrange equations, one can obtain the equation of motion:

$$M_I\dot{\boldsymbol{R}} \quad \sigma\boldsymbol{R}_I + \sum_{i,j}\Lambda_{ij}\frac{\partial}{\partial\boldsymbol{R}_I}\langle\varphi_i|\varphi_j\rangle - 2\sum_i\frac{\partial\langle\varphi_i|}{\partial\boldsymbol{R}_I}\left[\frac{\delta E}{\delta\langle\varphi_i|} - \sum_j\Lambda_{ij}|\varphi_i\rangle\right]. \tag{2.23}$$

Thus, orbitals must be reoptimized at each time step, which is computationally very costly for large-scale systems. But the BOMD can easily handle the 2D materials with moderate

computational cost because their reduced dimensionality. In my thesis, I used BOMD to investigate the thermal stability of 2D magnetic materials by Vienna *Ab initio* Simulation Package (VASP) software.[63]

2.6 General consideration for magnetic materials

Transition-metal (TM) cations with various oxidation state form TML_n polyhedra with surrounding main-group elements L (typically, n = 4–6). The *d* orbital in this polyhedra splits to different groups of unequal energies due to the crystal field effect (breaking of the spherical symmetry of the *d* orbital). Generally, the local magnetic moment for TM ions in solid state system can be understood by its spin states (high and low spin). According to the Griffth's theory of TM ions,[64] the spin states of TM ions is mostly determined by the relative magnitude of the crystal field splitting (Δ_{cf}) and exchange splitting (Δ_{ex}). For TM ions in a strong crystal field, $\Delta_{cf} > \Delta_{ex}$ case, TM ions will be in a low spin states breaking the Hund's rule. In contrast, for the weak crystal field $\Delta_{cf} < \Delta_{ex}$ case, the TM ions prefer to be in a high spin states following the Hund's rule. Moreover, the GGA and LDA level generally underestimate the exchange splitting for TM ions, and it results in an incorrect spin state. The DFT+U and hybrid-functionals can correct appropriately the exchange splitting and give an accurate local spin states for magnetic materials.[65,66,67]

The macroscopic magnetism of materials is derived from the spin-exchange interaction of TM ions. The spin-exchange interaction of TM ions generate the ferromagnetic, ferrimagnetic, and antiferromagnetic order in materials. The spin-exchange interaction, also called magnetic bonding, is weak compared to the chemical bonding. The strength of the magnetic bonding can be characterized by spin exchange parameter in materials and it can be described by model spin Hamiltonian:

$$H_{spin} = \sum_{i \neq j} J_{ij} \hat{S}_i \cdot \hat{S}_j \ . \tag{2.24}$$

The exchange-coupling parameter J_{ij} can be evaluated by energy-mapping analysis based on DFT total energy calculations, considering the different spin-configurations.[68] The Curie and Néel temperature of the FM and AFM materials are a reflection of the strength of the spin exchange parameter J_{ij}. The Curie and Néel temperature can be evaluated by the mean-field theory[69] and Metropolis Monte-Carlo simulations[70].

The mechanism of magnetic coupling can be understood by the competition between through-bond and through-space interactions of TM. For weakly interacting magnetic orbitals ϕ_1 and ϕ_2 on atoms the "molecular orbitals" ψ_1 and ψ_2 are separated by energy Δe as shown in Figure 2.1. The expression of energy difference between singlet states (Ψ_S) and triplet state (Ψ_T) was introduced by Roald Hoffmann et. al.[71] in 1975,

$$\Delta E = E(S) - \mathrm{E}(T) = -K_{12} + \frac{(\Delta e)^2}{U_{eff}}, \tag{2.25}$$

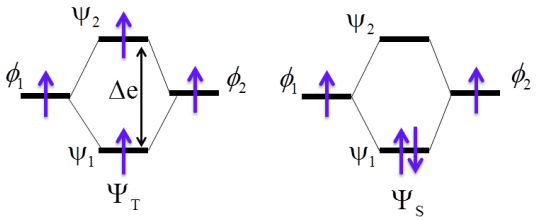

Figure 2.1: Singlet state and triplet state for spin-dimer.

where K_{12} is the exchange repulsion $K_{12} = \langle \phi_1(1)\phi_2(2)|1/r_{12}|\phi_2(1)\phi_1(2)\rangle$. U_{eff} is the effective on-site repulsion and Δe is the small energy gap between ψ_1 and ψ_2 due to the weak interaction as shown in Figure 2.1. Therefore, $\Delta E = E_{AFM} + E_{FM}$ and it follows that

$$E_{FM} = -K_{12} \text{ and } E_{AFM} = \frac{(\Delta e)^2}{U_{eff}}. \tag{2.26}$$

The FM term E_{FM} becomes stronger with increasing exchange integral K_{12} and it corresponds to the increase in overlap density $\phi_1\phi_2$ for TM dimer. The AFM term E_{AFM} becomes stronger with the increase of Δe, which depends on the overlap integral $\langle \phi_1 | \phi_2 \rangle$. The competition between through-bond (double exchange) and through-space (superexchange) interactions qualitatively originates from the competition between FM and AFM components. Mechanistic details can also be found in recent review by Xiang *et. al.*[68] Namely, when the interaction between TMs produces a large energy split Δe ($\langle \phi_1 | \phi_2 \rangle$), the through-space interaction is favorable. When the overlap density ($\phi_1\phi_2$) of TMs increases, the through-bond interaction is favorable. From the viewpoint of bonding theory, the through-bond spin polarization is an indirect interaction (double exchange) mediated by ligand atoms, while TM-TM direct spin polarization is a direct interaction through space. The mechanism of magnetic coupling in my thesis can be analyzed by the competition between through-bond (double

exchange) and through-space (superexchange) interactions. The calculations of magnetic properties for 2D materials were performd with VASP program using PBE, PBE+U and HSE06 functionals.

Chapter 3 Results and Discussion

3.1. Janus MXenes: spin-polarized semiconductors with zero magnetism

Searching for new materials with the high-spin polarization and a room-temperature magnetic order is essential for the development of the next-generation of spintronic devices. The materials with spin-polarized ferromagnetism have shown potential applications in spintronics as spin filters, detectors and sensors.[21,22] However, these ferromagnets usually have magnetic domains, a stray field and relatively low Curie temperature, all of that unavoidably restricting the generation of the spin-polarized current. The conventional antiferromagnetic materials have zero magnetization, insensitivity for stray field and high Néel temperature, whereas their spin channels are unfortunately degenerate. A new class of 2D magnetic materials with high Néel temperature, the fully compensated antiferromagnetic order (zero magnetization) and completely spin-polarized semiconductivity is proposed in this section. These materials are based on asymmetric functionalization of MXenes. Such materials show promising potential application in antiferromagnetic spintronics.

3.1.1 Structure, magnetic and electronic properties

The asymmetrically functionalized Cr-based MXenes are denoted Janus MXenes (Cr_2CXX', X, X'=H, OH, F, Cl, Br) throughout this thesis. The geometries of Cr_2CXX' materials together with their electronic and magnetic properties were investigated and they are summarized in Table 1. The calculated local magnetic moments show that Cr atoms are in the high spin (HS) state with $d^{3\uparrow}$ spin configurations and each Cr atom has a 3+ charge. The collinear FM, Néel, and zigzag states are considered as shown in Figure 3.1. The relative stability of FM states (E_{FM}), Néel states ($E_{Néel}$) and zigzag states (E_{zigzag}) are defined as: $\Delta E_{ex1} = E_{FM} - E_{Néel}$ and $\Delta E_{ex2} = E_{zigzag} - E_{Néel}$, respectively. A relative stability of the Néel state increases with increasing ΔE_{ex1} and ΔE_{ex2} values. It is found that the Néel states are stable in all Cr_2CXX' systems, similarly to previously reported results for symmetrically functionalized Cr_2CX_2.[23]

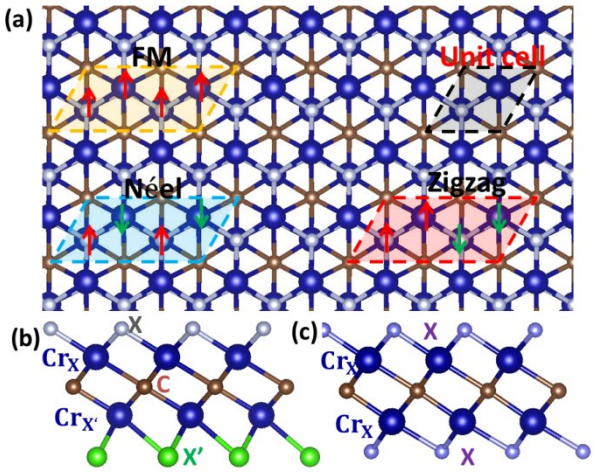

Figure 3. 1 A top and a side view of Cr2CXX' (parts a and b, respectively) and a side view of Cr2CX2 monolayer (c); The magnetic states are marked by yellow, cyan and red dotted lines.

Table 1 Calculated structural and magnetic characteristics of ten different Janus Cr_2CXX' MXenes.

Structure	L (Å)	ΔE_{ex1}(eV)	ΔE_{ex2} (eV)	J_1 (meV)	J_2 (meV)	T_N (K)
Cr_2CFCl	3.195	0.608	1.095	-22.534	19.155	395
Cr_2CHBr	3.206	0.442	0.855	-16.352	15.569	320
Cr_2CClBr	3.332	0.573	1.141	-21.211	21.088	385
Cr_2CFBr	3.252	0.530	0.677	-19.631	8.980	310
Cr_2CBrOH	3.259	0.524	0.659	-19.419	8.581	300
Cr_2CHCl	3.150	0.494	1.283	-18.292	26.487	430
Cr_2CHF	3.054	0.509	1.093	-18.846	20.974	380
Cr_2CClOH	3.203	0.594	1.049	-22.002	18.135	375
Cr_2CFOH	3.111	0.664	1.036	-24.580	16.496	390
Cr_2CHOH	3.066	0.460	0.481	-17.019	4.842	270

The nearest- and next-nearest-exchange coupling parameters J_1 and J_2 can be calculated by mapping the DFT energies to the spin Hamiltonian (Table 1). The Néel temperatures T_N

for Janus Cr_2CXX' are calculated from the spin Hamiltonian using the DFT derived spin exchange parameters and Monte-Carlo (MC) simulations. All Cr_2CXX' are have a high Néel temperature, suggesting potential applications in room-temperature electronic devices. The electronic property of Cr_2CXX' shows a bipolar antiferromagnetic semiconductor (BAFMS) coupling in which the valence band maximum (VBM) and conduction band minimum (CBM) states are 100% spin polarized with opposite spin channels. Similar to the definition of bipolar magnetic semiconductor (BMS),[6,7] the typical BAFMS can be described by three energy gaps (Δ1, Δ2 and Δ3) reported in Figure 3.2a. The Δ1 gap is defined as a spin-flip gap with the opposite spin polarization between VBM and CBM. In addition, one can manipulate the spin polarization of carriers in BMS simply by shifting the Fermi level. Following the notation of Refs. [6] and [7], the (Δ1+Δ2) and (Δ1+Δ3) are defined as spin-conserved gaps and Fermi level will shift up and down to be located in the Δ1 and Δ3 gaps in a positive and negative gate voltage, respectively. Calculated Δ1, Δ2, and Δ3 gaps are 1.02, 0.31, and 0.41 eV, respectively, for Cr_2CFCl, (see Figure 3.3 for Δ values of other MXenes).

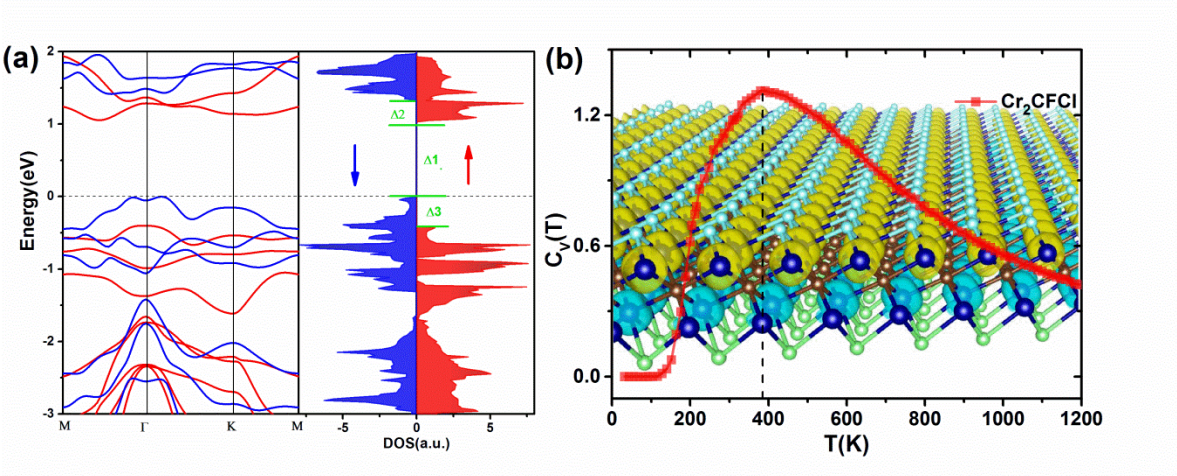

Figure 3. 2 (a) Band structure and total DOS for Cr_2CFCl. (b) Simulated specific heat C_V as a function of temperature (T) for Cr_2CFCl. The inserted background figure shows spin polarized charge densities of Cr_2CFCl.

3.1.2. Manipulation with the orientation spin-polarization

The spin-polarization direction of BAFMS materials can be controlled easily by electron and hole doping, which can be realized by a gate voltage in practical applications. The doping electron and hole will shift the Fermi level to different spin-polarized VBM and CBM regions. For small electron doping, the Cr_2CFCl changes from a BAFMS to half-metal

antiferromagnets (HMAFM) with spin-down polarization, while a spin-up polarized HMAFM state is obtained in the case of hole doping. Thus, completely spin-polarized currents with tunable spin orientation of carriers and HMAFM properties can be realized by applying either an electron or hole doping. The tunable spin-polarization direction provides a potential strategy to manipulate the carrier spin-polarization in 2D Janus MXenes simply by applying a gate voltage.

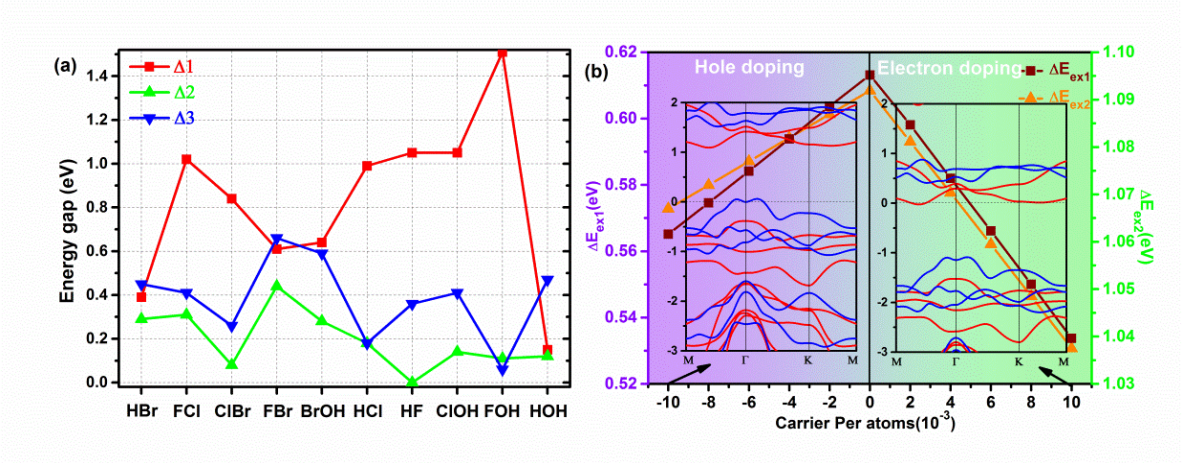

Figure 3. 3 Spin-flip gaps and spin-conserved gaps for Cr_2CXX' Janus MXenes (a). ΔE_{ex1} and ΔE_{ex2} as a function of carrier concentration calculated for Cr_2CFCl (b). The calculated band structures for electron doping and hole doping;

3.1.3. The origin of electronic structure

To understanding the BAFMS properties of Cr_2CXX', the partial electronic density of states (PDOS) of Cr_F and Cr_{Cl} atoms of Cr_2CFCl (Figure 3.4) are discussed below. The spin up *d* states of the Cr_{Cl} atom mainly lie within (-4, 0) eV and (1, 2) eV energy windows, whereas some spin-down *d* states mostly corresponds to unoccupied states above the fermi level. The crystal field and exchange splittings of Cr_{Cl}-*d* states are 1.75 and 2.18 eV, respectively, and for Cr_F –*d* states they are 1.87 eV and 1.45 eV, respectively. The differences in crystal and exchange field splittings on Cr_F and Cr_{Cl} ions (due to the differences in chemical environment of these ions) result in different values of splitting parameters. This give rise to the mismatch of *d* states, which further induce the spin-polarized effect in Cr_2CFCl materials. The other Cr_2CXX' materials can be understood by the same mechanism.

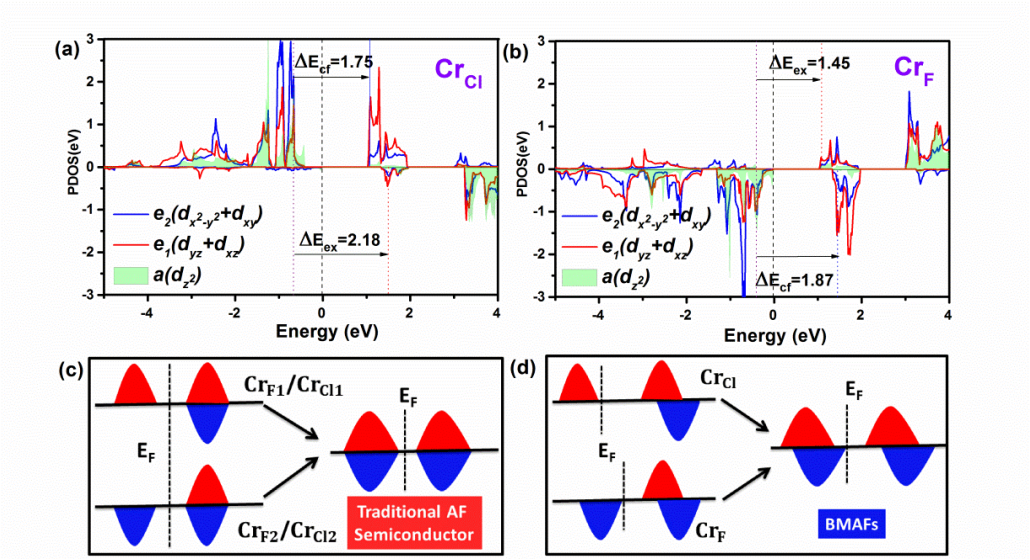

Figure 3. 4 PDOS of *d* states for Cr_{Cl} (a) and Cr_F (b) calculated for Cr_2CFCl. Schematic diagrams of the Cr spin exchange splitting in symmetrically and asymmetrically functionalized surfaces are shown in parts (c) and (d), respectively.

The origin of AFM order of Cr_F and Cr_{Cl} in Cr_2CFCl is discussed next. The spin-polarized charge densities (SCD), electron localization functions (ELF) and schemes of the exchange mechanism are plotted in Figure 3.5 for Cr_2C and Cr_2CFCl. ELF maps show that the Cr_2C and Cr_2CFCl have distinct characteristics of *d* orbitals: itinerant *d* electrons for Cr_2C and localized *d* electrons for Cr_2CFCl. Itinerant *d* electrons can induce the spin-polarization of neighboring C atoms (C shows the spin-polarization in SCD figure) and Cr_2C maintains the AFM coupling between the Cr and the neighboring C atoms. They can form the spin arrangement like $Cr_1\uparrow-C_\downarrow-Cr_2\uparrow$.[72] Therefore, the FM coupling of Cr ions in Cr_2C is mediated by C-2*p* states via double-exchange mechanism (Figure 3.5a). However, for Cr_2CFCl, the local Cr_{Cl}-*d* orbitals can directly induce the antiparallel spin arrangement on neighboring Cr_F ($Cr_{Cl}\uparrow-Cr_F\downarrow$ configuration) via the super-exchange mechanism as shown in

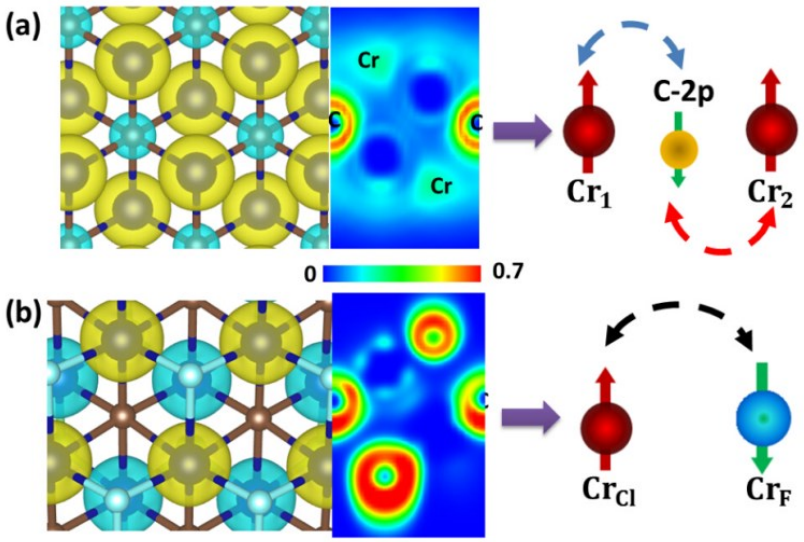

Figure 3. 5 The spin-polarized densities (SCD), electron localization functions (ELF) and schemes of the exchange mechanism for Cr_2C (a) and Cr_2CFCl (b) are presented.

3.1.4. Dynamical and thermal stability

The formation energies of asymmetrically functionalized Cr_2CXX' (Figure 3.6a) are just in between formation energies of corresponding symmetrically functionalized Cr_2CX_2 MXenes. These results indicate the formation of strong chemical bonds between the transition metals and the functional groups and they are consistent with the fact that chemically functionalized MXenes were synthesized experimentally.[21,22] The 2x2 supercell with various F and Cl composition ($Cr_8C_4F_mCl_n$ (n, m = 0, 1, …, 4)) is always thermodynamically favorable compared with the pristine Cr2C for a range of F and Cl chemical potentials

To confirm the dynamical stability of Cr_2CFCl material, its phonon dispersion curves were calculated (Figure 3.6d). The absence of imaginary frequencies proves that Cr_2CFCl monolayer is dynamically stable. Furthermore, to evaluate the thermal stability of the Cr_2CFCl material, the *ab initio* molecular dynamics (AIMD) simulations were also performed at 300 K in a canonical ensemble using the Nosé heat bath. Results reported in Figure 3.6c indicate that the atomic structure of the Cr_2CFCl remains intact at 300 K for the duration of the simulation (more than 8 ps with a time step of 2 fs). Only a small variation of the total potential energy along the simulation time suggests that Cr_2CFCl is thermally stable at room temperature.

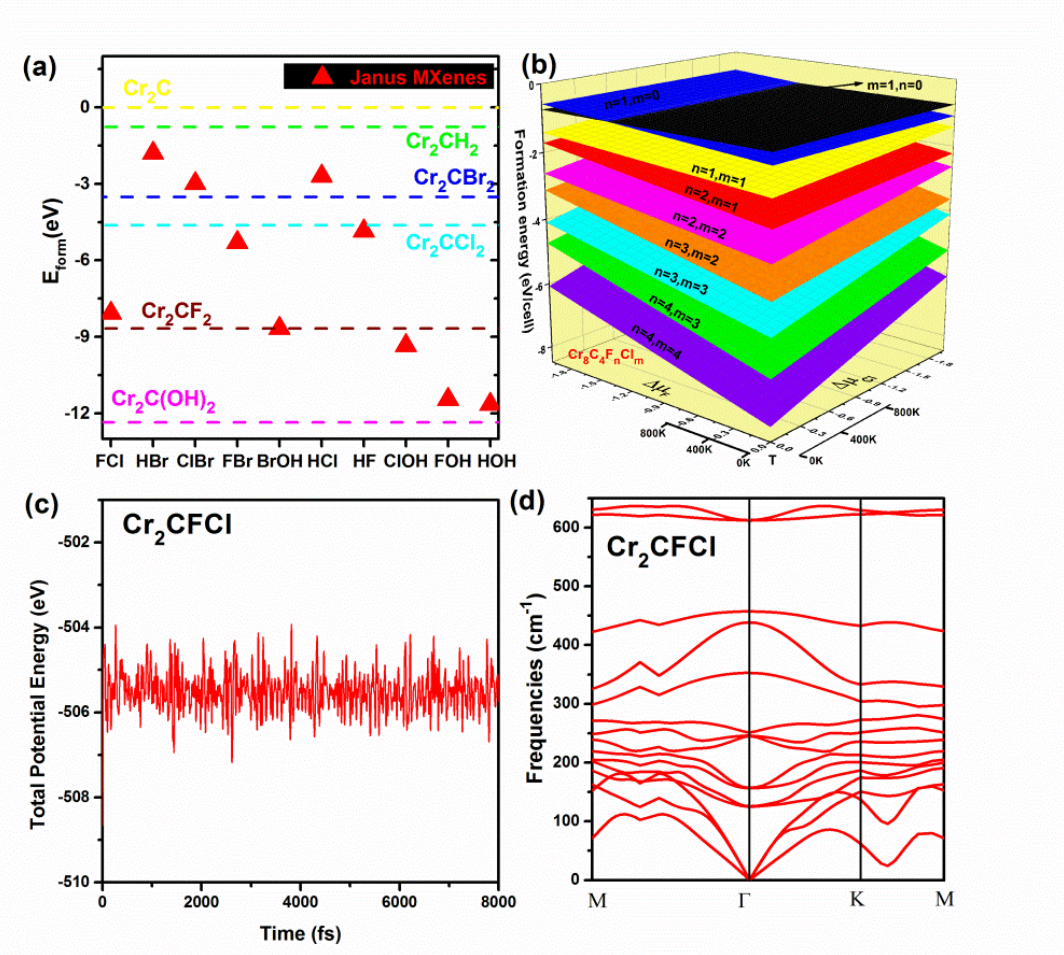

Figure 3. 6 (a) Formation energies, Cr_2CX_2 and Cr_2CXX'. (b) Formation energies $Cr_8C_4F_nCl_m$ (n, m = 0, 1, ..., 4) with various F/Cl chemical potentials. (c) Variations of the total potential energy at 300 K. (d) Phonon dispersion

3.1.5. Mixed functionalization and substrate effect

The Janus Cr_2CXX' with the perfectly asymmetrical functionalization of upper and lower surfaces is an ideal system. The most relevant system synthesized until today is Ti-based MXene obtained by exfoliation in hydrogen fluoride solution where both surfaces are functionalized randomly by H and F atoms.[73,74] it is therefore important to investigate electronic properties of variously substituted surfaces that are far from ideal situation described above. Three model situations were investigated and the results are reported in Figure 3.7. First, starting from the symmetrically substituted Cr_2CF_2 MXene, a single F atom on upper surface was replaced by a Cl atom; such isolated Cl surface atom was considered (varying the supercell size) for Cl coverages 11 and 25% (Figure 3.7a). Second, starting from the symmetrically substituted Cr_2CF_2 MXenes, several adjacent F atoms on upper surface

were replaced by Cl atoms (forming a Cl island) considering 33, 56, and 67% coverage of Cl on the upper surface (Figure 3.7b). Third, starting from perfectly asymmetrical substitution of Cr_2CFCl, one, two, and three (randomly selected) F atoms from the upper surface where switched with the corresponding number of Cl atoms from the lower surface (Figure 3.7c). All considered model situations show completely compensated AF ground states and the spin-polarized semiconductor behavior. It leads to an important conclusion that mixed functionalization of Cr_2C is sufficient to affect the chemical environment of Cr atoms in upper and lower surfaces enough to observe BAFMS characteristics.

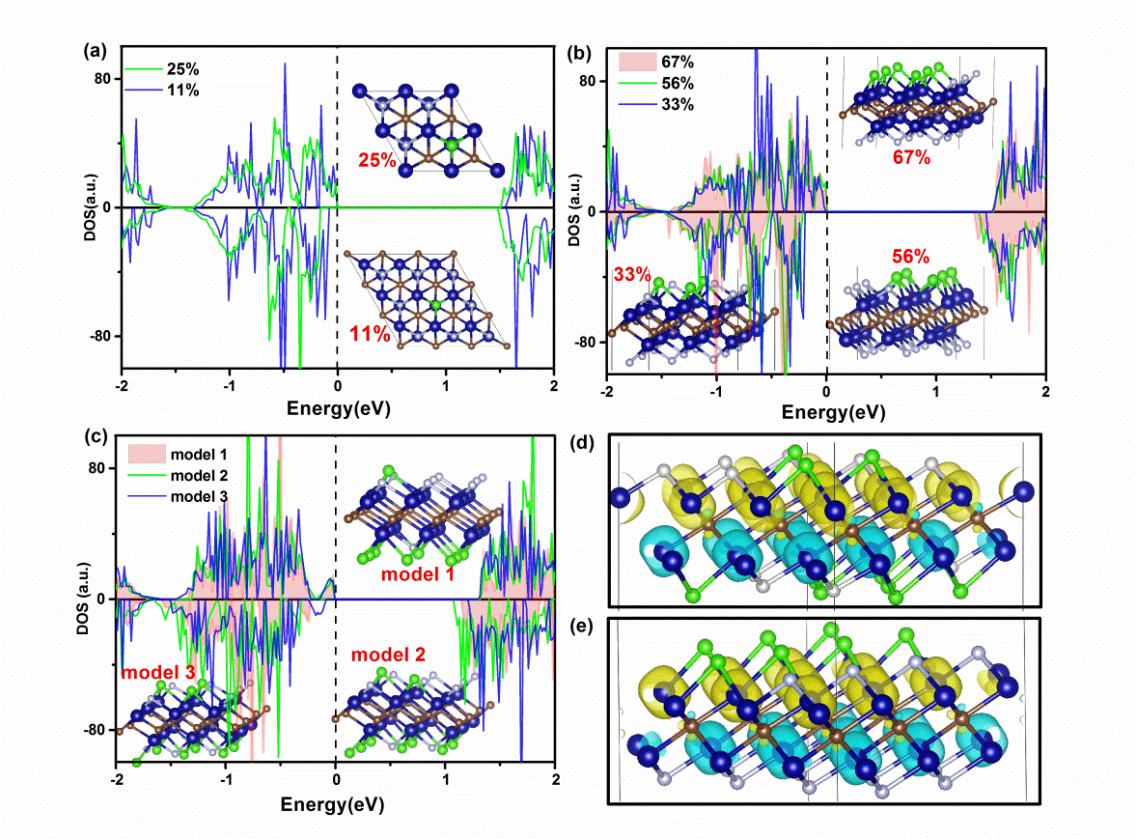

Figure 3. 7 DOS for various $Cr_2CF_xCl_y$ systems. (a) A single Cl atom on the upper surface of Cr_2CF_2. (b) Cl islands on upper surface of Cr_2CF_2. (c) Cr_2CFCl with randomly switched F/Cl atom(s). (d) and (e) The spin-polarized charge density (SCD)

The results reported above were obtained for the models representing free-standing MXenes. The effect of the MXenes interaction with the substrate (unavoidable in potential applications) on the electronic structure and compensated AFM couplings is discussed below. The Cr_2CF_2 and Cr_2CFCl MXenes on SiC(0001) were investigated for the case of hydrogen saturated SiC(0001) surface. The distance between MXenes and substrate is 2.76 and 2.57 Å for Cr_2CF_2 and Cr_2CFCl, respectively, indicating just a weak van-der-Waals bonding. The

Cr_2CF_2 and Cr_2CFCl on SiC(0001) retain the compensated antiferromagnetic coupling as shown in Figure 3.8. The DOS of Cr_2CF_2 with symmetrical distribution indicates no spin polarization, while the Cr_2CFCl maintains the BAFMS features. These results show that the asymmetrically functionalized Cr_2CXX' retain BAFMS features even if they interact with the substrate, the conclusion important for potential applications in nanoelectronic devices.

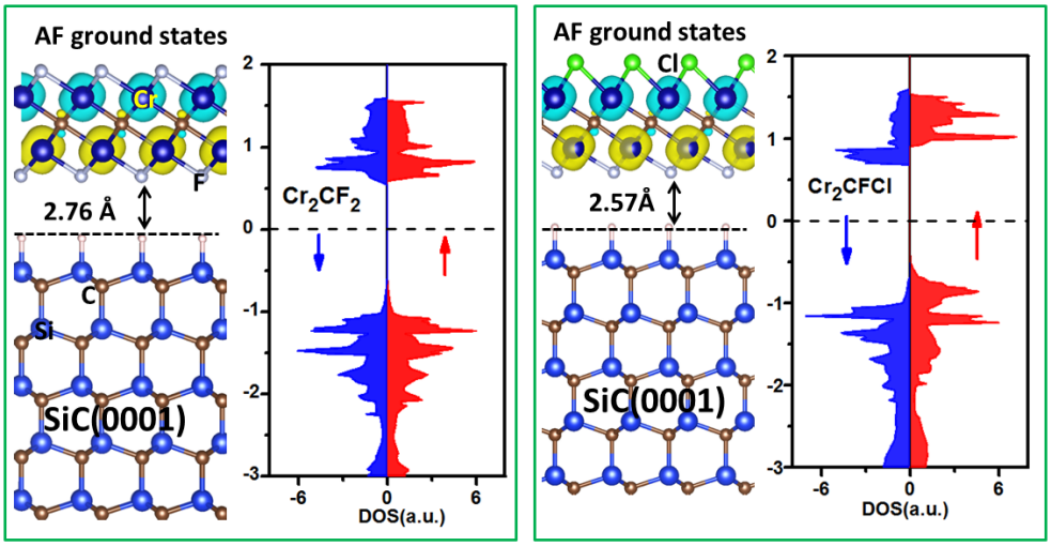

Figure 3. 8 DOS of Cr_2CF_2 (a) and Cr_2CFCl (b) supported on SiC(0001) substrate.

3.1.6. Summary

In this section, a new class of 2D magnetic materials – asymmetrically functionalized MXenes with high Néel temperature, fully compensated antiferromagnetic order, and completely spin-polarized semiconductivity – is proposed for the first time. The valence and conduction bands in these materials are made up of opposite spin channels and these materials show BAFMS characteristics. These BAFMS characteristics result from: (i) the asymmetrical functionalization of upper and lower Cr_2C surfaces inducing the *d* states mismatch on Cr sublattice, (ii) Cr atoms maintain a perfect AFM super-exchange interaction. The band gap of Janus MXenes can be effectively tuned to different regions by a selection of a suitable pair of chemical elements (groups) terminating upper and lower surfaces. It is also shown that BAFMS characteristics are present even in $Cr_2CF_xCl_y$ systems with mixed functionalization The application of electron and hole doping allows an easy control of the spin carriers orientation, leading to the transition from BAFMS to HMAFMs, which could be realized experimentally through the gate voltage. Our results provide a general strategy to identify the

2D high-temperature antiferromagnetic spin-polarized materials from transition-metal based layered materials.

3.2 Mn-based MXenes: half-metallicity and room-temperature ferromagnetism

Two-dimensional transition metal carbides (MXenes) have attracted great attention due to their potential applications in sensors, catalysis, energy storage and nanoelectronics. Previous investigations have demonstrated that Ti, Ta and Cr based MXenes have magnetic properties. However, the magnetism of MXenes generally disappears when their surfaces are chemically functionalized due to the completely compensated antiferromagnetic (AFM) ground states, which will limit MXenes broader application in spintronics. A new magnetic Mn_2GaC MAX phase was recently predicted theoretically and subsequently synthesized as a thin film with ferromagnetic order.[75,76,77,78] It remains to be seen whether Mn_2GaC MAX phase can be experimentally converted to 2D Mn_2CT_2 MXene in analogy with several MAX phases that have been transformed into Ti_2CT_2 and V_2CT_2 MXenes. In this section, we investigated the electronic and magnetic properties of two-dimensional Mn_2CT_2 (T = F, Cl, OH, O, and H) MXenes based on the computational approach. While other two dimensional MXenes become non-magnetic upon symmetrical functionalization of their surfaces, the Mn_2C MXene functionalized with functional groups bearing formal charge -1 (F, Cl, and OH) retains ferromagnetic ground state upon functionalization. These magnetic properties make the Mn_2CF_2 MXene an optimal material for applications in spintronics.

3.2.1 Structure and stability

The initial structure of 2D MXene was obtained simply by removing the Ga layer from the bulk Mn_2GaC MAX phase. The 2D Mn_2C forms a hexagonal layer with C_{3v} symmetry as shown in Figure 3.9; C atoms are sandwiched between two layers of Mn atoms. After exfoliation of bulk MAX phase by HF acid solutions, it is expected that the surfaces of Mn_2C are terminated with chemical elements/groups, *e.g.*, F in case of HF solution, the case that has been found experimentally for Ti_2CF_2 and V_2CF_2 MXenes. The geometry optimization of 2D Mn_2CF_2 gives lattice parameters 3.10 Å. The calculated Mn_2CF_2 formation energy (-8.63 eV) is relatively large, indicating a formation of strong chemical bonds between Mn and F atoms

and thermodynamic feasibility. Moreover, *ab initio* molecular dynamic calculations show that the Mn_2CF_2 monolayer is thermally stable at 500 K (Figure 3.10a). The phonon spectra shown in Figure 3.10b show no negative frequency phonons at the whole Brillouin zone. All these results indicate that the Mn_2CF_2 MXenes monolayers are dynamically stable and they could exist as free-standing 2D monolayers.

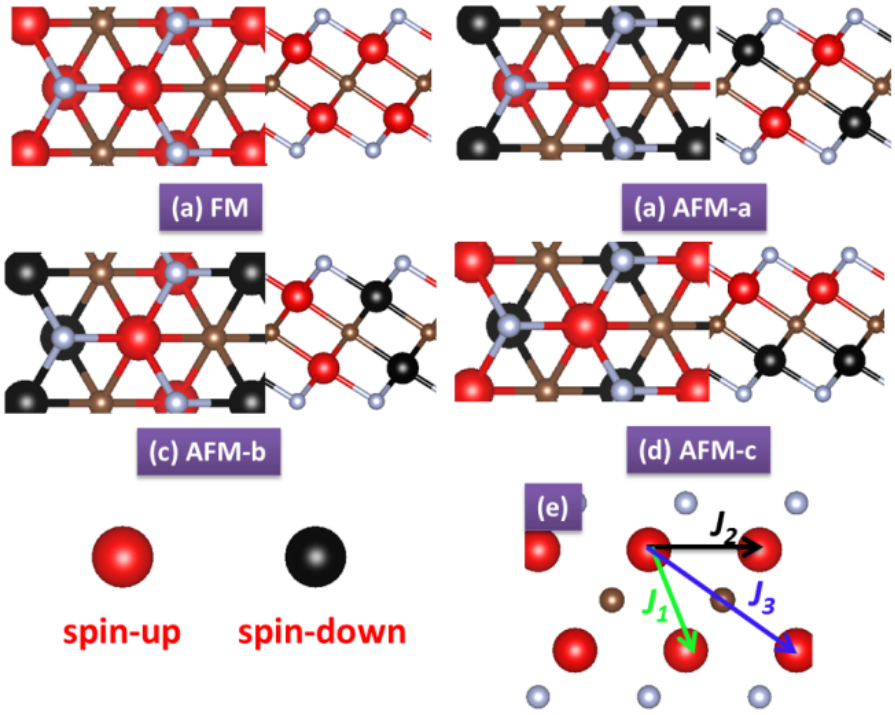

Figure 3. 9 Possible magnetic configurations: FM (a), AFM-a (b), AFM-b (c), and AFM-c (d). The spin exchange path (e) for J_1, J_2 and J_3 are also marked.

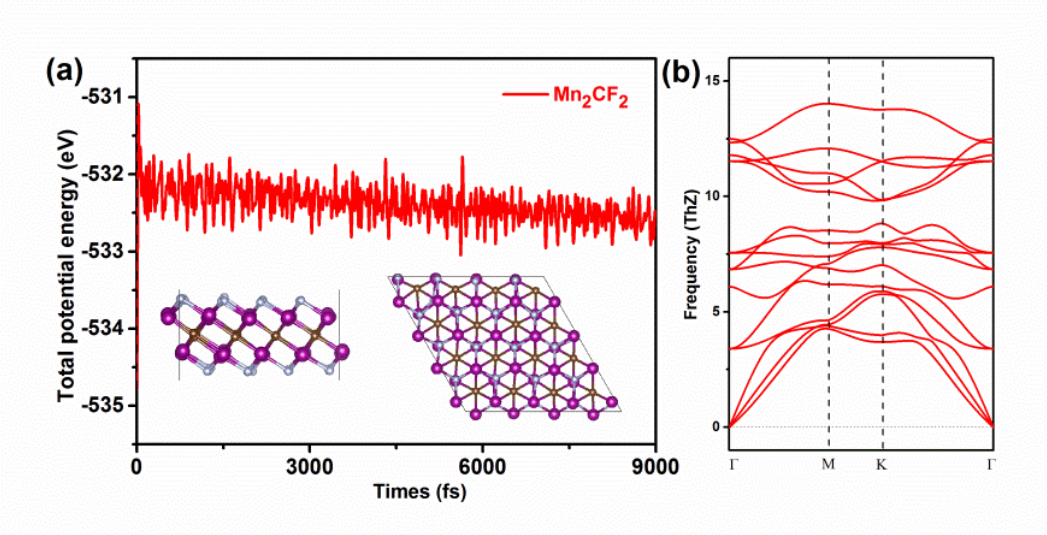

Figure 3. 10 (a) Variations of the total potential energy during *ab initio* molecular dynamics simulations at 500 K. (b) Phonon dispersion curves

3.2.2 Electronic structure, magnetism and magnetic anisotropy

The FM states of Mn_2CF_2 MXenes have total magnetic moment 8 μ_B (per unit cell), that is mainly contributed by Mn atoms. Each Mn atom has a magnetic moment of 4.15 μ_B, that can be expected for a formally Mn^{3+} electronic configuration, and there is -0.43 μ_B on C atoms. To study the magnetic ground state structures of Mn_2CF_2 monolayer, the collinear ferromagnetic state, and AFM states (AFM-a, AFM-b and AFM-c define in Figure 3.9) were considered. The lowest energy has been found for the FM state and this has been set as reference energy. The results clearly demonstrate that the FM state configuration of the Mn_2CF_2 monolayer is the magnetic ground state with high magnetic stability. The calculated nearest- , next-nearest- and next-next-nearest-neighbors exchange-coupling parameters (J_1, J_2, and J_3) are 6.8, -0.1 and 17.1 meV, respectively. The Curie temperature derived from these exchange-coupling parameters is calculated to be 520 K for Mn_2CF_2, which is higher than for a majority of previously studied 2D magnetic materials.[79] This value is similar to previously calculated T_C = 660 K for corresponding Mn_2GaC MAX phase.[76]

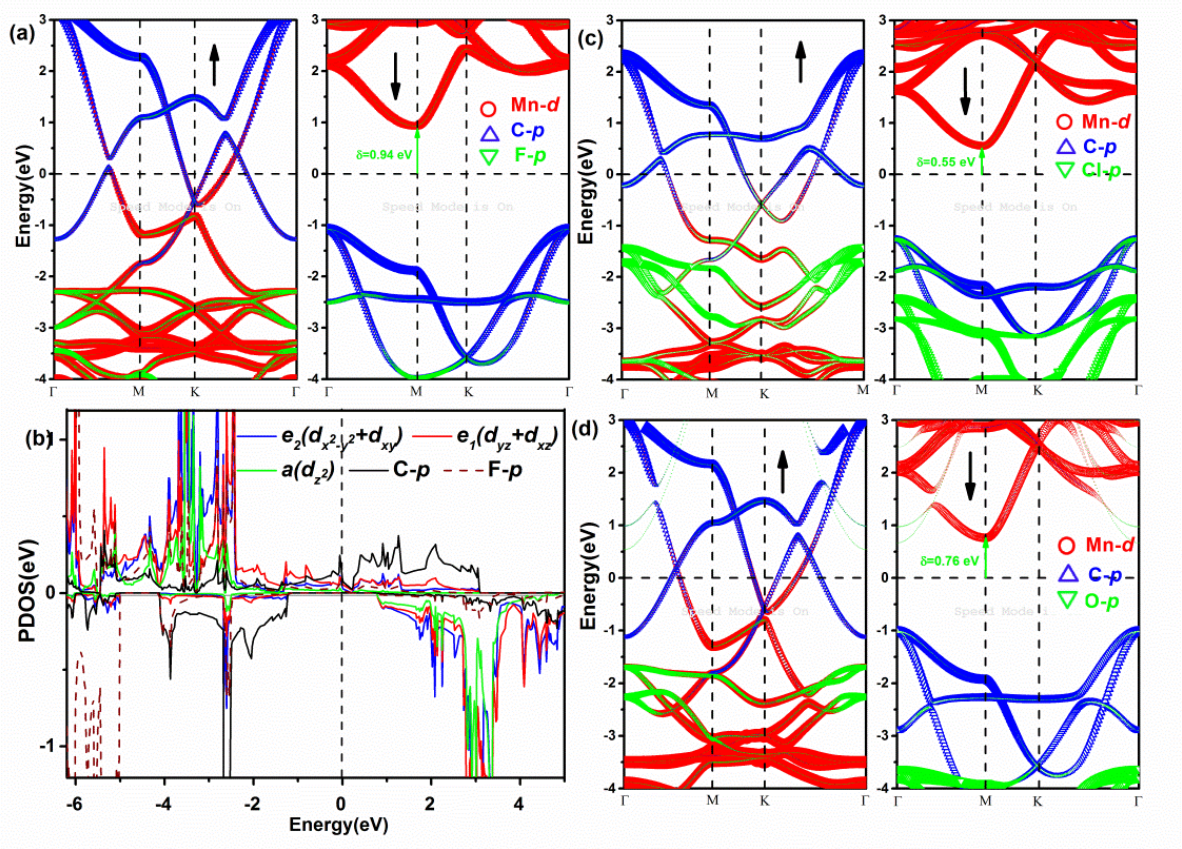

Figure 3. 11 Band structure with the orbital weights for Mn_2CF_2 (a), Mn_2CCl_2 (b) and $Mn_2C(OH)_2$ (d). PDOS showing Mn *d* states (b).

The band structure of Mn_2CF_2 obtained at the PBE+U level is shown in Figure 3.11. The calculated band structure clearly shows half-metallic character (energy gap for minority-spin electrons and metallic character for majority-spin electrons) leading to 100% spin-polarized electrons at the Fermi level. The half-metallic gap is defined as the spin-flip transition energy from a majority- to a minority-spin channel (denoted δ in Figure 3.11). A large half-metallic gap can efficiently prevent the spin flip transitions and can guarantee the half-metallic character. The half-metallic gap calculated for Mn_2CF_2 (0.94 eV at PBE+U level) is larger or comparable to those reported for double perovskites, chalcogenides and similar materials.[80,81]

The non-collinear magnetic calculations were performed for magnetization along X [100], Y [010] and Z [001] directions, where *Z* is the surface normal. The energy difference between X (Y) and Z directions is denoted E_{XZ} (E_{YZ}). The easy magnetization axis is Z [001]. The calculated magnetic anisotropy energy (MAE) E_{XZ} =E_{YZ} = 24 μeV/(Mn atom) is similar to those reported for 2D materials previously.[82] And it is order of magnitude larger than found for commonly used ferromagnetic materials such as bulk Fe (1.4 μeV per atom) and bulk Ni (2.7 μeV per atom).[83]

The structural, thermodynamic, electronic and magnetic properties of Mn_2CT_2 MXenes (X = Cl, OH, O, H) were investigated computationally following exactly the same approach as reported above for Mn_2CF_2; results are reported in Figure3.11 and Table 2. Magnetic properties depend primarily on the formal oxidation state of surface functional species. For Mn_2C surfaces functionalized by functional groups bearing (-1) formal charge (F, Cl, and OH), the net magnetization per unit cell is 8 μ_B and they are all ferromagnetic half metals with similar (but different) magnetic characteristics (Table 2). Calculated Curie temperatures (520, 460 and 380 K for Mn_2CF_2, $Mn_2C(OH)_2$ and Mn_2CCl_2, respectively) are all well above the room temperature. For the Mn_2C surface functionalized by O atoms (formal charge -2) and by H atoms (formal charge +1), the net magnetization drops to 6 μ_B and resulting 2D materials are no longer half metals. The changes in magnetic ground states in Mn_2CT_2 MXenes result from the changes in electron acceptor/donor characteristics of the surface functional group. Moreover, all Mn_2CT_2 materials investigated herein have an easy magnetization axis along Z [001] with considerable MAE as shown in Table 2.

3.2.3. The origin of electronic and magnetic properties

Partial electronic density of states (PDOS) of Mn_2CF_2 is shown in Figure 3.11b for Mn-based MXenes. The atomic and orbital resolved band structures show that both Mn(*d*) states and C(*p*) states contribute to half-metallic states near the fermi level. The states of Mn atom can be divided into two parts: first, localized states with energies below -2 eV; second, delocalized *d* states with energies ranging from -2 eV to 2.5 eV. One can see that the metal states in the spin up channel near the Fermi level are derived mainly from delocalized Mn(*d*) and C(*p*) states. A majority of Mn(*d*) states is below the Fermi level and only minority of Mn(*d*) states is just above the Fermi level. Such electronic structure corresponds to Mn3+ ions which are also consistent with a total 8 μ_B spin magnetic moment per unit cell. Similarly, Mn atoms in the Mn_2C and Mn_2CO_2 MXenss can be formally considered as Mn^{2+} and Mn^{4+} ions, respectively. The microscopic origin of various magnetic couplings in Mn-based MXenes can be understood in terms of two competing interactions, i.e., the direct exchange through space (M-M direct) and superexchange through bond (M-C-M indirect).

Table 2 Calculated structural and magnetic characteristics of five different Mn_2CT_2 MXenes.

[a] L is the lattice constant (in Å). [b] E_{form} is the formation energy. [c] M is the magnetization per unit cell. [d] Relative energies for FM (E_{FM}) and AFM ($E_{AFM\text{-}a}$, $E_{AFM\text{-}b}$ and $E_{AFM\text{-}c}$) states are in eV. [e] $T_{C/N}$ stands for the Curie and Néel temperatures, respectively (in K). [f] The magnetic anisotropy in μeV.

Structure	L[a]	E_{form}[b]	M[c]	E_{FM}[d]	$E_{AFM\text{-}a}$	$E_{AFM\text{-}b}$	$E_{AFM\text{-}c}$	$T_{C/N}$[e]	E_{YZ}[f]	E_{XZ}[f]
Mn_2CF_2	3.11	-8.63	8	0	0.415	1.842	2.295	520	24	24
Mn_2CO_2	2.95	-12.22	6	0.056	0.338	0	0.161	110	90	91
$Mn_2C(OH)_2$	3.17	-14.22	8	0	0.407	1.810	2.021	460	19	26
Mn_2CCl_2	3.35	-4.74	8	0	0.347	1.971	2.137	380	37	38
Mn_2CH_2	2.89	-0.90	6.06	0.059	0	0.325	0.763	120	233	233

3.2.4 Summary

A new type of 2D Mn_2CT_2 MXenes investigated herein computationally shows unique electronic and magnetic features, very advantageous for potential applications in spintronics. The most important features of Mn_2CT_2 MXenes include:

(i) The Mn_2CT_2 MXenes retain FM ground state even upon the symmetrical functionalization of surfaces with groups bearing -1 formal charge (F, Cl or OH). These are the first and only functionalized MXenes with FM ground states reported so far.

(ii) The thermal and dynamic stability have been confirmed by the *ab-initio* molecular dynamic calculations and phonon spectra calculations.

(iii) Magnetic properties of Mn_2CT_2 MXenes can be modulated by the surface functional group. Depending on the electronegativity of functional group these MXenes can be either FM half metals, AFM metals, or AFM semiconductors.

Our results indicate that new 2D Mn_2CT_2 materials have magnetic features ideal for applications in spintronincs: tunable magnetic order including half metallicity, high Curie temperature and magnetic anisotropy.

3.3 Vanadium halide monolayer: Dirac half-metallicity and intrinsic ferromagnetism

The 2D Dirac materials exhibit novel physical properties such as linear band dispersion, ballistic charge transport, enormously high carrier mobility, and topological phases. The key point for practical applications in spintronic devices is to develop 2D materials with ordered spin structure and 100% spin polarization. Half-metals with one conducting spin channel and one insulating/semiconducting spin channel have been considered as the ideal materials for spintronic applications. By combining the two fascinating properties of massless Dirac fermions and 100% spin polarization, the Dirac half-metallicity (DHM) has been predicted by us for VCl_3 and VI_3 layered materials based on DFT+U methods. The stability and electronic and magnetic structure of VCl_3 and VI_3 monolayers were systematically investigated at the DFT+U level. The results show that VCl_3 and VI_3 monolayers have intrinsic ferromagnetism and Dirac half-metallicity. Our results greatly broaden the family of potential 2D Dirac materials. Calculated properties of VCl_3 and VI_3 monolayers show that these materials have a

great application potential, opening the way towards the development of high-performance electronic devices.

3.3.1 Cleavage energy and structure stability

The VCl_3 and VI_3 layered materials have a rhombohedral BiI_3 crystal structure type with the R3 space group. V atoms (with d^2 spin configurations) are arranged in a honeycomb lattice. To explore a possible exfoliation of a monolayer from the bulk structure of VCl_3 and VI_3, cleavage energies were calculated as shown in Figure 3.12. The calculated cleavage energies are 0.11 and 0.18 J/m^2 for VCl_3 and VI_3, respectively. The results are comparable with the CrX_3 (X=Cl, Br, I) materials, which have been exfoliated experimentally.[36] Consequently, these results suggest that VCl_3 and VI_3 monolayers can be possibly obtained by exfoliation process from their layered bulk phases. To further confirm the stability of VCl_3 and VI_3 monolayers, their phonon spectra were calculated (Figure 3.13). There are no negative frequency phonons found at the whole Brillouin zone. The results indicate that the VCl_3 and VI_3 monolayers are dynamically stable. Moreover, AIMD calculations carried out for 9 ps (with a time step of 3 fs) show that both VCl_3 and VI_3 layers are stable. Variations of the total potential energy with respect to the simulation time (Figures 3.13) are almost invariant during the simulation, suggesting that the VCl_3 and VI_3 monolayers are thermally stable at room temperature.

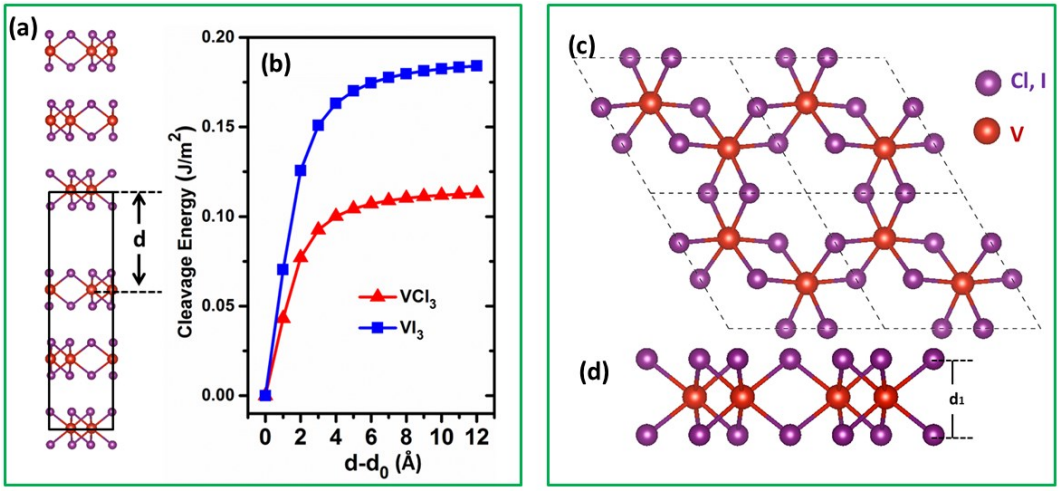

Figure 3. 12 Bulk model (a) of VX_3 (X = Cl, I) and the cleavage energy (b) d_1 represents the equilibrium interlayer distance of chromium trihalides.

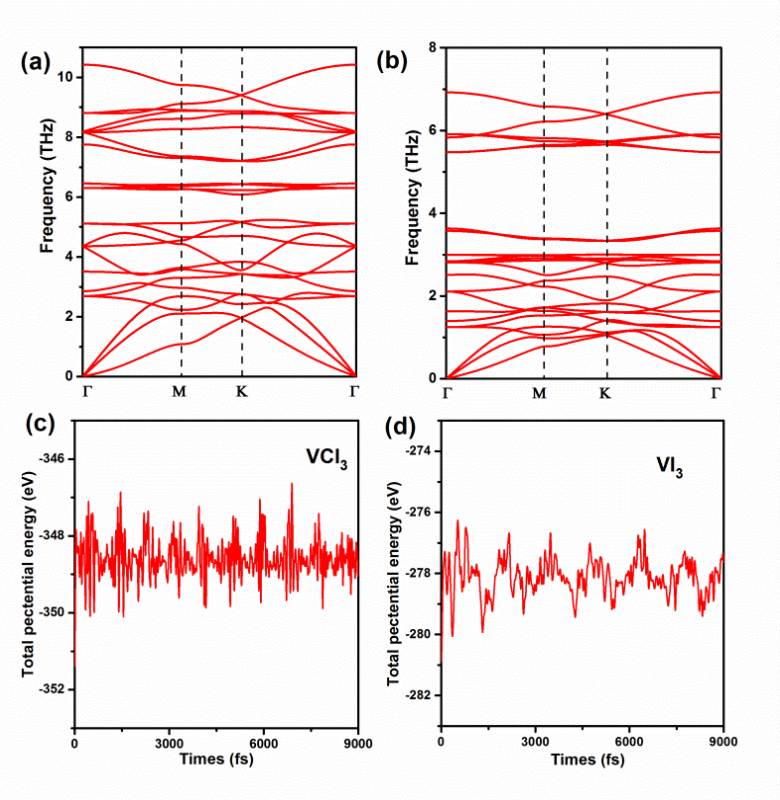

Figure 3. 13 Phonon band structures of (a) VCl_3, and (b) VI_3, respectively. Variations of the total potential energy of VCl_3 (c) and VI_3 (d) along AIMD simulations.

3.3.2 Magnetic ground states and electronic structure.

The FM states of VCl_3 and VI_3 have total magnetic moments 4 μ_B (per unit cell). V atoms dominantly contribute to the total magnetic moments while the neighboring X atoms have only a little contribution. To determine the preferred magnetic ground state structures of VCl_3 and VI_3 systems, the collinear FM, Néel, zigzag and stripy states are considered as shown in Figure 3.14. The FM states are found to be the most stable magnetic configurations. Calculated exchange coupling parameters of VCl_3 and VI_3 are summarized in Table 3. The first neighboring J_1, and the third neighboring J_3 exchange parameter for both VCl_3 and VI_3 are ferromagnetic. The second exchange parameter (J_2) for the next-nearest neighbors is ferromagnetic for VCl_3, while it is weekly antiferromagnetic for VI_3 monolayer. However, it should be noted that J_1 is one order of magnitude lager than J_2 and J_3. The Curie temperatures T_C for VCl_3 and VI_3 are estimated to be 80 K and 98 K by Monte Carlo (MC) simulations, for VCl_3 and VI_3 monolayers, respectively.

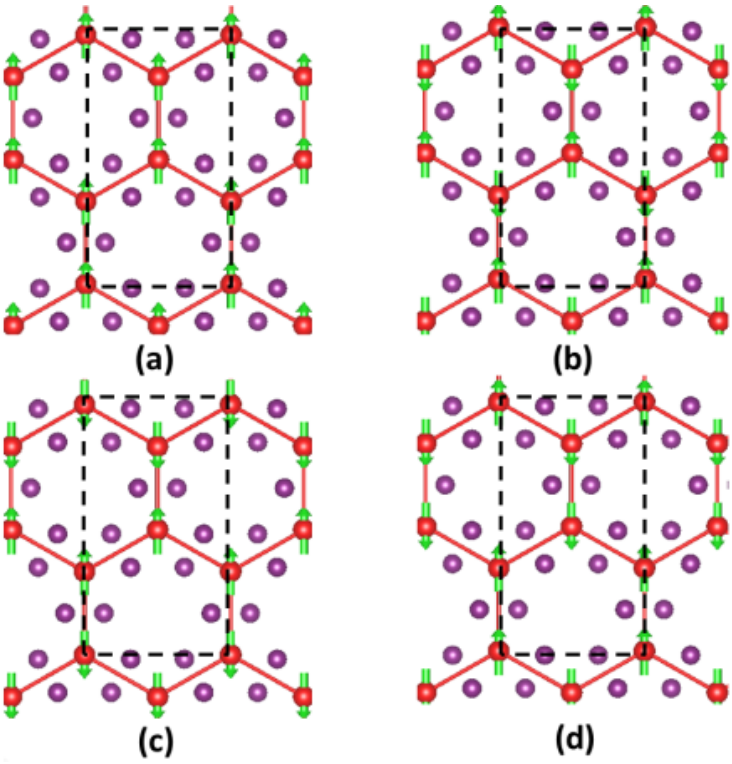

Figure 3. 14 The possible magnetic configurations of a single VX_3 (X=Cl, I) layer.

Table 3 Calculated characteristics of VCl_3 and VI_3 monolayers.

L is the lattice constant, d_1 is the vertical distance between two halide planes, $d_{V\text{-}X}$ and $d_{V\text{-}V}$ represent the bond length of V-X and V-V, respectively. The 'U' is the U parameter calculated by linear response method.

Structure	L Å	d_1 Å	$d_{V\text{-}X}$ Å	$d_{V\text{-}V}$ Å	U (eV)	J_1 (meV)	J_2 (meV)	J_3 (meV)	T_C (K)
VCl_3	6.28	2.76	2.42	3.66	3.35	2.227	0.144	0.02	80
VI_3	7.18	3.30	2.81	4.14	3.68	2.754	-0.019	0.110	98

The electronic band structures and density of states (DOS) of VCl_3 and VI_3 are depicted in Figure 3.15. Both 2D materials reported herein show half-metallic character and they can be used as ideal spin-filter devices, moreover, they both show rather unusual Dirac half-metallicity. A linear dispersion relation near the Fermi level indicates that the spin-polarized massless Dirac fermions are found in the spin up channels of VCl_3 and VI_3 at the high-symmetry *K* point of the Brillouin zone. The Dirac points located at *K* for VCl_3 and VI_3 are

just 20 and 106 meV above the Fermi level, respectively. The calculated Fermi velocities (υ_F) of Dirac fermions using $\upsilon_F = \partial E(k)/\partial(\hbar k)$ are about 0.16 × 10^6 and 0.1 ×10^6 m/s for VCl_3 and VI_3 monolayers, respectively, values high enough for the applications as high-speed electronic devices.

The partial electronic density of states (PDOS) is calculated for VX_3 monolayer to gain insight into the origin of Dirac states (Figure 3.16). It clearly shows that most of Cl and I atomic states are located in the lower energy range of the valence band and in the higher energy range of the conduction band, while these states contributes to the states near the fermi level with only little weight. On the contrary, the V states have high weights near the Dirac states. The Dirac states of VCl_3 and VI_3 are mainly derived from the V-*d* states, where the X-p_z (X=Cl, I) do not contribute significantly. Compared with *p* electrons Dirac materials such as graphene, the *d*-orbital Dirac materials have in general a stronger spin exchange interaction and a larger spin-orbit coupling (SOC). The SOC-induced gaps are calculated to be 29 meV and 12 meV for VCl_3 and VI_3 structures, respectively. Moreover, the origin of ferromagnetism in VCl_3 and VI_3 can be understood by a double-exchange mechanism.

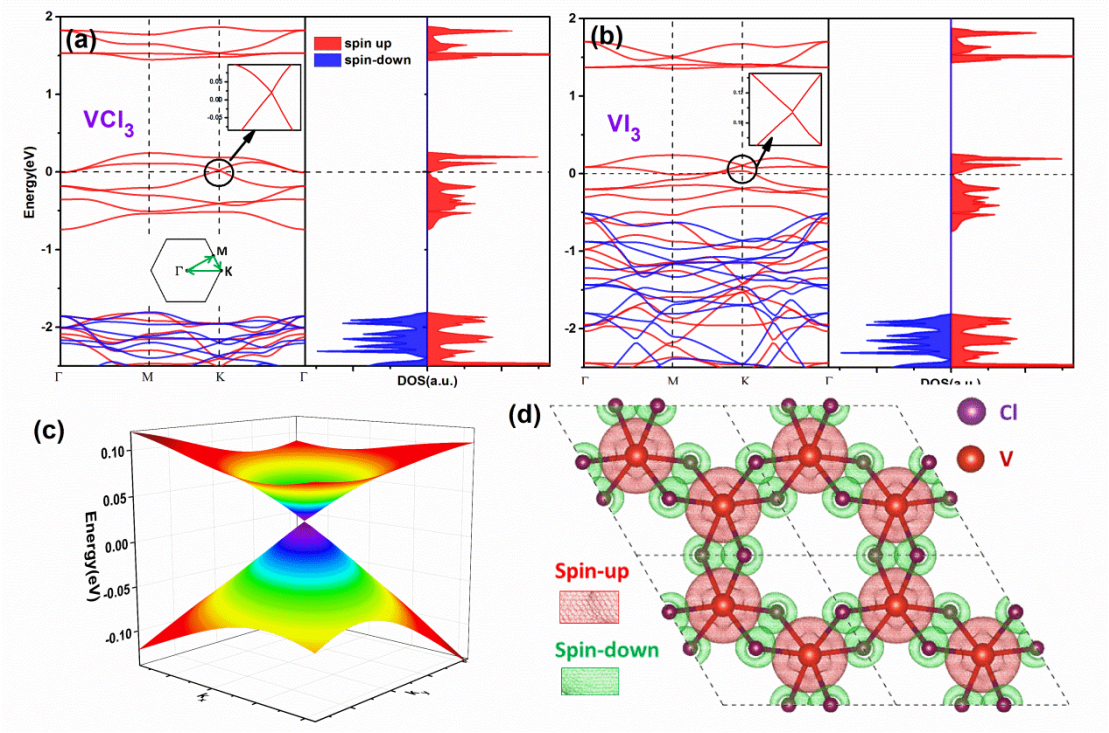

Figure 3. 15 Band structure and total DOS for VCl_3 (a) and VI_3 (b). The 3D Dirac band structure for VCl_3 (c) and Spin-polarized charge densities of VCl_3 (d)

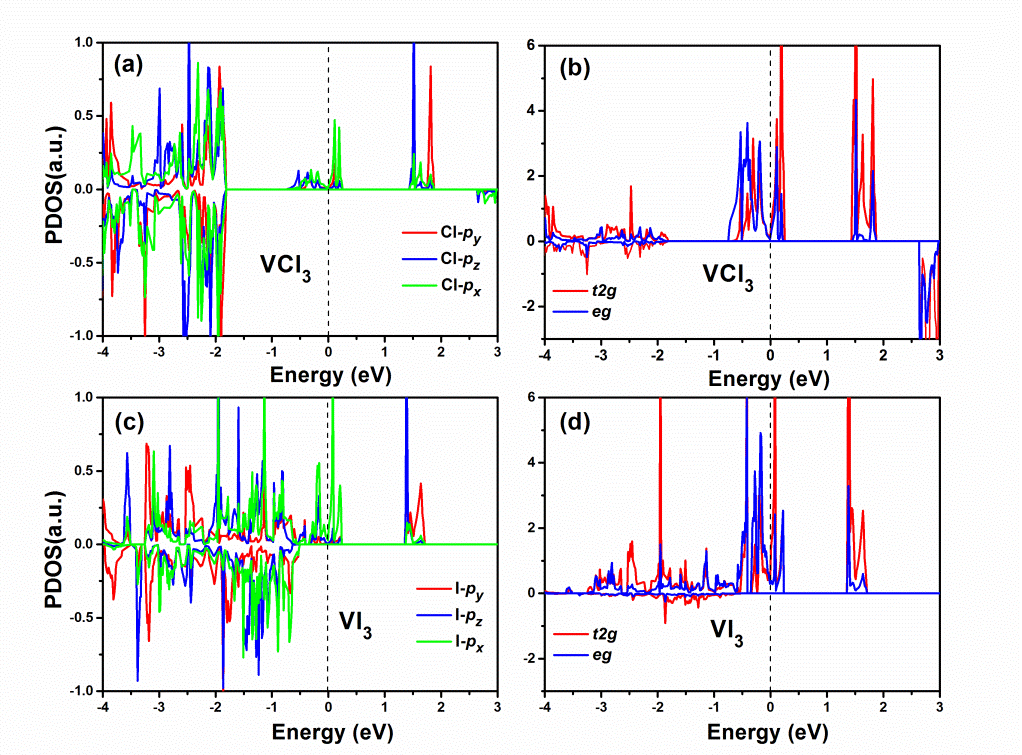

Figure 3. 16 PDOS of Cl (a) and V (b) atoms of VCl_3 monolayer and PDOS of I (c) and V (d) atoms of VI_3 monolayers are shown.

3.3.3 Tuning the Curie temperature and Dirac states

The Dirac states for VCl_3 and VI_3 are not located exactly at the fermi level. They are just 20 and 106 meV above the Fermi level for VCl_3 and VI_3 monolayers, respectively. A suitable doping can move the Fermi level downwards to shift the Dirac states of VCl_3 and VI_3 materials exactly at the Fermi level as shown in Figure 3.17. Moreover, the Curie temperatures of VCl_3 and VI_3 monolayers is far below room temperature, it is thus important to examine if the carrier doping can lead to a Curie temperature increase. Both the electron and hole doping are effective ways to improve ferromagnetism of VCl_3 and VI_3 monolayers up to a room-temperature. At the same time, for electron doping levels of 0.1 and 0.7 per unit cell for VCl_3 and VI_3 monolayer, respectively, the Dirac states are exactly located at the Fermi level. The carrier doping is usually implemented experimentally by a gate voltage. Therefore, it will be possible to apply a gate voltage to control the ferromagnetism and Dirac states.

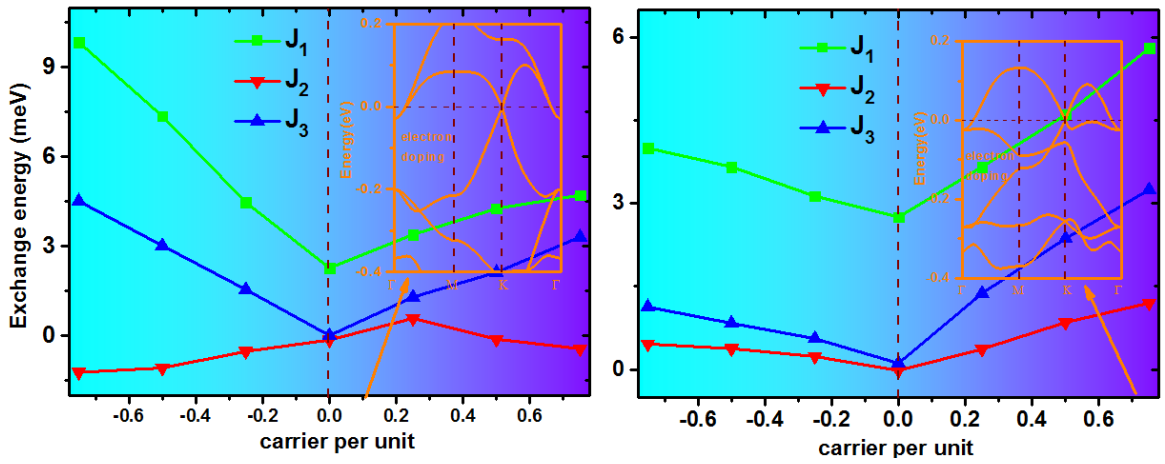

Figure 3. 17 The spin exchange parameters as a function of carrier concentration calculated for VCl_3 (a) and VI_3 (b). The band structures in electron doping presented in the insets.

3.3.4 Summary

The stability, electronic and magnetic structures of VCl_3 and VI_3 monolayers was systematically investigated by DFT+U approach. The feasibility of exfoliation from their layered bulk phases is predicted computationally based on rather small cleavage energies. The phonon calculations suggest that single layers of VCl_3 and VI_3 are dynamically stable and that they can exist as freestanding 2D crystals. DFT+U indicate that VCl_3 and VI_3 monolayers show an intrinsic ferromagnetism and the half-metallicity. Remarkably, the VCl_3 and VI_3 monolayers possess exciting half-metallic Dirac point around Fermi level with just one spin channel. Contrary to the *p*-state character of the Dirac point in graphene, the Dirac points in VCl_3 and VI_3 monolayers are mainly due to the V-*d* states and consequently they show stronger spin-couplings than found in graphene. The Monte Carlo simulations based on the Ising model demonstrate that the Curie temperature of VCl_3 and VI_3 layers are 80 K and 98 K, respectively. The carrier doping not only can effectively control the ferromagnetism and increase further the Curie temperature up to the room temperature, but it can also shift the Dirac states with respect to the Fermi level. Our results greatly broaden the family of 2D Dirac materials and opens up possibilities for developing high-performance electronic or spintronic devices.

3.4 Nickle chloride monolayers: near room-temperature Chern insulator

The Chern insulator, a material which can realize the quantum anomalous Hall (QAH) effect, have attracted a great research interest. The QAH effect have been observed experimentally in the topological insulator Cr doped $(Bi,Sb)_2Te_3$ film[84] at extremely low temperature (below 30 mK) due to only a weak magnetic coupling and a corresponding small band gap. A great obstacle for practical applications of the QAH effect is the lack of suitable Chern insulator with a large non-trivial band gap, room-temperature magnetic order and high carrier mobility. Based on the first principles calculations it is shown here that a nickel chloride ($NiCl_3$) monolayer has all these characteristics – high-temperature ferromagnetism, large non-trivial band gap and Dirac fermions. And it gives this material a great potential for a realization of the near-room temperature QAH effect and potential applications in spintronics.

3.4.1 Structure, mechanical properties and stability

The structure of $NiCl_3$ monolayer is shown in Figure 3.18a. Ni atoms form a 2D honeycomb lattice and each Ni atom is bonded to six Cl atoms in an octahedral environment. Geometry optimization carried out at PBE level gives lattice constant 5.966 Å (Figure 3.18b). The calculated 2D Young's modulus 25 N/m for $NiCl_3$ monolayer is very close to values obtained previously for V- and Cr-based chlorides and it is about 7% of the in-plane stiffness of the graphene (340 N/m).[85] One phonon band (Figure 3.19) has quite small imaginary frequencies (~0.02 Thz) in the vicinity of the Gamma point ($k \rightarrow 0$), which can be caused by the numerical inaccuracy due to the limited supercell size. Such modes are of acoustic nature and they are derived from a collective vibrational mode with a long wavelength approaching infinity.[86,87] which will not significantly affect the overall structural stability of $NiCl_3$ monolayer. Moreover, AIMD calculations carried out for 9 ps (with a time step of 3 fs) at 500 K show clearly that the $NiCl_3$ monolayers are thermally stable at room temperature. Most importantly, the system remains magnetic throughout the simulation with an average supercell magnetic moment of about 18 μ_B (2 μ_B per unit cell), demonstrating that magnetic state of $NiCl_3$ is robust at room temperature.

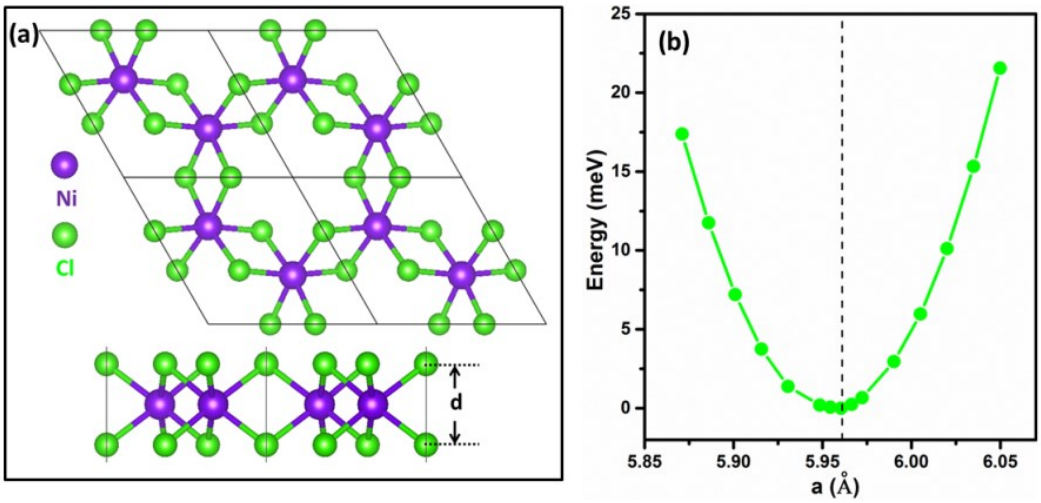

Figure 3. 18 (a) The top and the side views of the optimized $NiCl_3$. (b) Variation of total energy with the lattice constant.

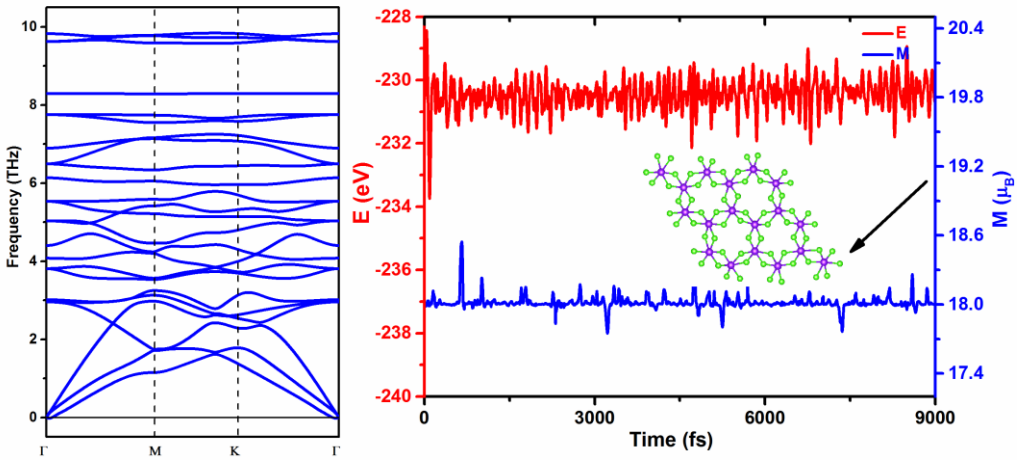

Figure 3. 19 (a) Phonon band structure; (b) potential energy (E) and total magnetic moment (M) fluctuations during the AIMD simulation.

3.4.2 The electronic and magnetic properties

The spin-polarized FM ground state with a total magnetic moment of 2 μ_B per unit cell was found for $NiCl_3$. Based on the Monte–Carlo simulations the $NiCl_3$ monolayer have been predicted to have ferromagnetic ground states with 400 K Curie temperature, orders of magnitude higher than temperature for the experimentally observed QAH effect. The $NiCl_3$ monolayers can be a potential candidate for the high temperature QAH effect in spintronic applications. The band structure of the $NiCl_3$ FM ground state is shown in Figure 3. 20. The spin-down channels of $NiCl_3$ possess a 1.22 eV and 4.09 eV band gap at PBE and HSE06 levels, respectively, whereas the spin-up channel shows a gapless semiconductor feature with

a linear dispersion relation around the Fermi level. The spin-polarized massless Dirac fermions are found in the spin up channels of $NiCl_3$ at the high-symmetry *K* point of the Brillouin zone. The electronic structure of $NiCl_3$ show rather rare Dirac spin-gapless semiconductor characteristics that are essential for potential high-speed spin filter devices. The calculated Fermi velocities (v_F) of Dirac fermions are about 4×10^5 m/s for $NiCl_3$ monolayers at HSE06 level, a value that is approximately half of that found for graphene (8×10^5 m/s).

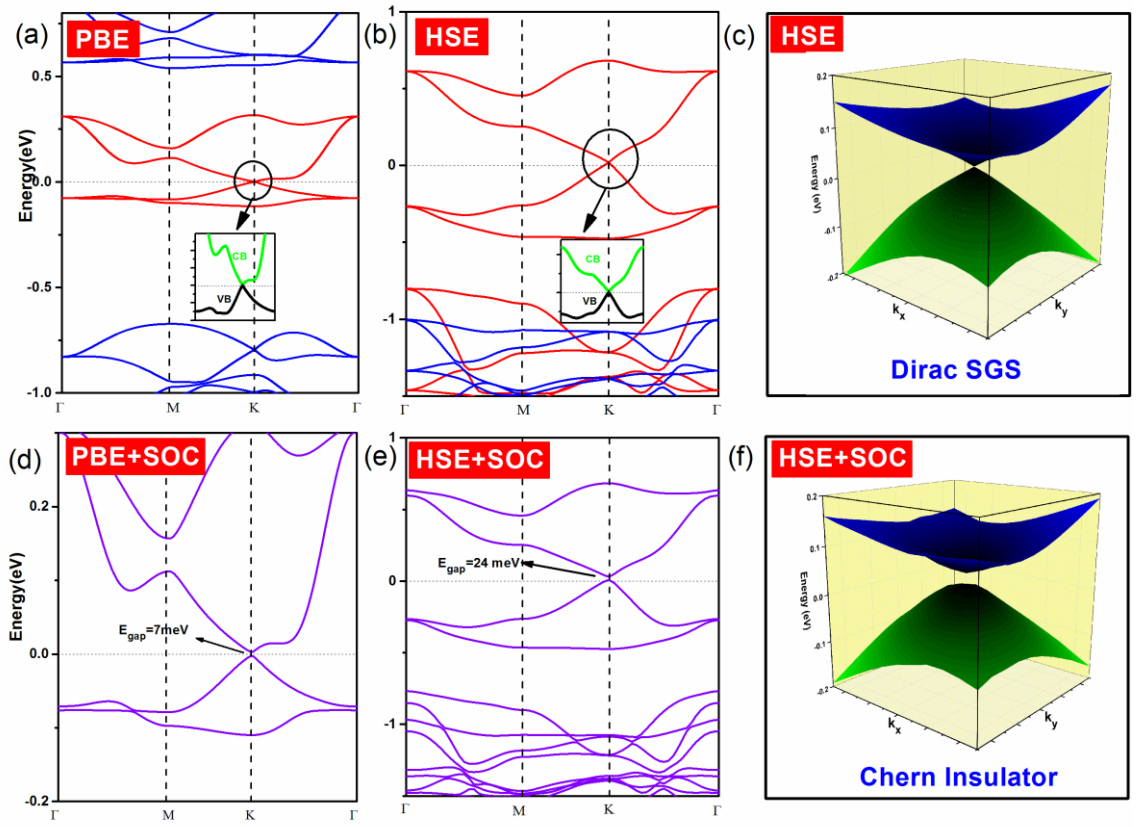

Figure 3. 20 Band structures of 2D $NiCl_3$ with (a) and without (b) SOC calculated at the PBE and HSE levels. The 3D band structures obtained without (c) and with (f) SOC.

3.4.3 Quantum anomalous Hall states

The Dirac states of $NiCl_3$ are mainly derived from the Ni-*d* orbitals, which shows stronger SOC than *p*-orbital in Graphene. The larger SOC gap of Ni-*d* orbitals with the broken time reversal symmetry (TRS) may lead to the Chern insulator and QAH effect. The SOC gap was calculated by relativistic PBE+SOC calculations to be 7 meV (Figure 3.20). However, SOC gaps calculated at the HSE06 level are considered more reliable and they are often comparable with experimental values. The HSE06+SOC calculations show the 24 meV gap

which is sufficiently large for the QAH effect to be operative at the temperature as high as 280 K. The Chern insulator states of $NiCl_3$ monolayer can be confirmed by the non-zero Chern numbers. The Berry curvature $\Omega(\vec{\kappa})$ along the high-symmetry direction (*M'-K'- Γ-K-M)* have two sharp spikes of the same sign located at the *K* and *K'* points as shown in Figure 3.21a. By integrating the Berry curvature in the entire Brillouin zone, the calculated Chern number *C* is -1 with non-trivial topological states. As expected from the non-zero Chern number, the anomalous Hall conductivity shows a quantized charge Hall plateau of $\sigma_{xy} = Ce^2 / h$.

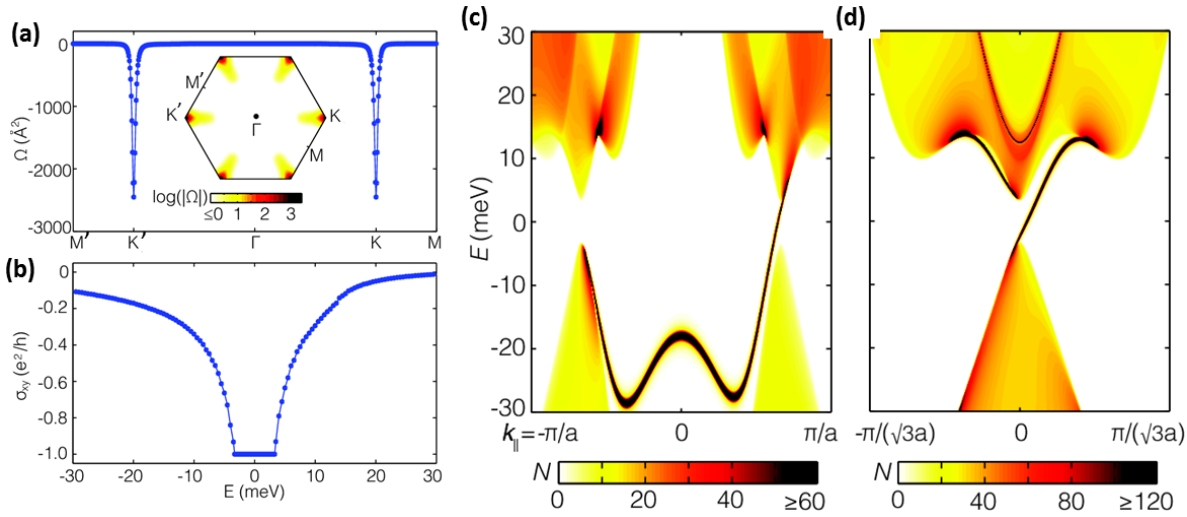

Figure 3. 21 (a) The distribution of the Berry curvature. (b) QAH conductivity. Calculated edge states for (c) Zigzag and (d) armchair insulators.

The existence of topologically protected chiral edge states is one of the most important consequences of the QAH state. We calculate the edge states of $NiCl_3$ monolayer with zigzag and armchair insulators using Green's functions based on Wannier functions[88,89] obtained from PBE calculations. As shown in Figure 3.21, the nontrivial edge states (dark line) connecting the valence and conduction bands cross the insulating gap of the Dirac cone. The appearance of only one chiral edge state is consistent with the calculated Chern number $C = -1$, confirming the nontrivial topological nature of $NiCl_3$ monolayer. The single spin Dirac fermion mediated topological properties of the $NiCl_3$ monolayer show a great potential to generate the QAH effect.

Finally, the PDOS and orbital-projected band structures around Fermi level were calculated for $NiCl_3$ monolayer to gain insight into the origin of magnetic and topological properties (Figure 3.22). Under the distorted octahedral crystal field of Cl atoms, the d orbital

of Ni would be split into $e_1(d_{xz}, d_{yz})$, $e_2(d_{xy}, d_{x^2-y^2})$ and $a_1(d_{z^2})$ states. The partially occupied e_1 and e_2 orbitals around the Fermi level form a Dirac point in the $NiCl_3$ monolayer. The states near the Fermi level are dominated by e_2 orbitals with only small contribution from e_1 orbitals. Without SOC, both VB and CB show equivalent weight for e_1 and e_2 states. Calculations with SOC show significantly increased contributions of both e_1 and e_2 in CB while the e_1 and e_2 contributions to VB decrease. As a result, the degeneracy of e_1 levels (and similarly the degeneracy of e_2 levels) around the Dirac point is lifted, opening thus a global energy gap between CB and VB bands (Figure 3.22b). The SOC results in the significant changes of e_1 and e_2 orbital energies and their contributions to CB and VB and consequently it plays a crucial role for the topological property of $NiCl_3$ monolayer.

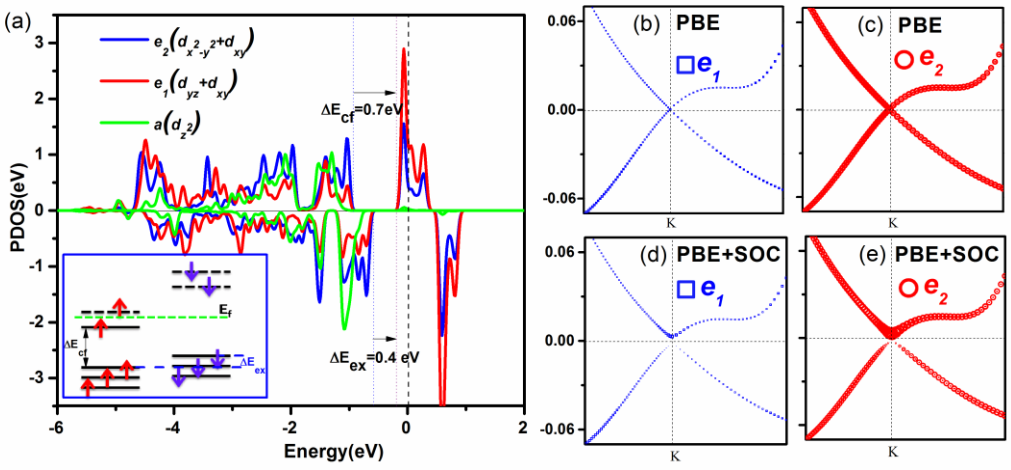

Figure 3. 22 (a) PDOS of Ni atom *d* states. The evolution of orbital-resolved band structures without (b), (c) and with (d) (e) SOC .

3.4.4 Summary

The stability and electronic and magnetic properties of $NiCl_3$ monolayers was systematically investigated at the DFT level of theory. The thermal and dynamical stabilities have been confirmed by phonon calculations and *ab initio* molecular dynamics simulations. The $NiCl_3$ monolayers show the Dirac spin-gapless semiconducting characteristics and high-temperature ferromagnetism (~400 K). In addition, a Fermi velocity in $NiCl_3$ monolayer is calculated to be 4×10^5m/s, which is comparable to graphene (8×10^5 m/s). Taking the spin-orbit coupling into account, the $NiCl_3$ monolayer becomes an intrinsic Chern insulator with a large non-trivial band gap of about 24 meV, corresponding to an operating temperature of 280 K. The

large non-trivial gap, high Curie temperature and single-spin Dirac states for $NiCl_3$ monolayers give a rise to great expectations for both the realization of near room temperature QAH effect and potential applications in spintronics.

Chapter 4 Conclusion

The requirement of continuous reduction of size of nanoelectronic device stimulate the development of new magnetic materials with the low-dimensionality, high spin-polarization and intrinsic magnetic order. The aim of the presented thesis was to discover computationally new 2D magnetic materials with novel electronic and magnetic properties, such as the bipolar antiferromagnetic semiconductor, half-metal, Dirac half-metal and Chern insulator. Our finding not only greatly broaden the 2D materials family for spintronics applications, but enrich the type of magnetic materials in general. The essential findings of our studies can be summarized as follows:

We proposed new types of 2D materials with coexistence of zero magnetism and spin-polarized semiconductivity by using asymmetrical and mixed functionalization of MXenes. The valence and conduction bands in these materials are made up of opposite spin channels and these materials show bipolar antiferromagnetic semiconductor characteristics. The application of electron and hole doping leads to an easy control of the spin carriers orientation, leading to the transition from bipolar antiferromagnetic semiconductor to half-metal antiferromagnets, which could be realized experimentally through the gate voltage. The spin-polarized semiconductivity with zero magnetism is preserved when MXenes are put on the SiC(0001) support.

We investigated the electronic and magnetic properties of new two-dimensional Mn-based MXenes (Mn_2CT_2,T = F, Cl, OH, O, and H). Our results show that they are intrinsic half-metal with high Curie temperature (520 K), wide half-metallic gap (0.9 eV) and a sizable magnetic anisotropy (24 μeV). These magnetic properties make the Mn_2CF_2 MXene an optimal material for applications in spintronics. Different surface functional groups lead to either quantitative (Cl and OH) or qualitative (O and H) changes of Mn_2CT_2 magnetic properties. It is proposed that Mn_2CT_2 MXenes can be prepared experimentally from already an existing parent Mn_2GaC MAX phase by exfoliation techniques.

We investigated systematically the stability, electronic and magnetic structure of VCl_3 and VI_3 layers. Our results show that VCl_3 and VI_3 have intrinsic ferromagnetism and half-metallicity with rather rare single spin Dirac point. Contrary to the Dirac point in graphene, the Dirac points in VCl_3 and VI_3 monolayers are mainly due to the V-*d* electrons and consequently they show a large spin-orbital coupling induced gaps of about 29 meV and 12

meV, respectively. The feasibility of an exfoliation from VCl_3 and VI_3 layered bulk phases is confirmed by small cleavage energies. Our results greatly broaden the family of potential 2D Dirac materials, opening the potential way towards the development of high-performance electronic devices.

We investigate the electronic, magnetic and topological insulator properties of $NiCl_3$ monolayer. $NiCl_3$ monolayer is found to be a new class of Dirac materials with Dirac spin-gapless semiconducting properties and high-temperature ferromagnetism. Moreover, taking into account the spin-orbit coupling, the $NiCl_3$ monolayer becomes an intrinsic Chern insulator with a large non-trivial band gap of ~24 meV, corresponding to an operating temperature as high as ~280 K at which the quantum anomalous Hall (QAH) effect could be observed. The novel transport properties for QAH effect have been confirmed by the topological edge states calculation.

Results reported in this thesis were published in four papers that are included as an attachment and where more details can be found.

References

[1] Wolf, S. A. D.; Awschalom, D.; Buhrman, R. A.; Daughton, J. M.; von Molnr, S.; Roukes, M. L.; Chtchelkanova, A. Y.; Treger, D. M. *Science* **2001**, *294*, 1488–1495.

[2] Žutić, I.; Fabian, J.; Sarma, S.D. *Rev. Mod. Phys.* **2004**, *76*(2), 323.

[3] De Groot, R.A.; Mueller, F. M.; Van Engen, P.G.; Buschow, K. H. J. *Phys. Rev. Lett.* **1983**, *50*(25), 2024.

[4] Wang, X. L. *Phys. Rev. Lett.* **2008**, *100*, 156404.

[5] Hu, X. *Adv. Mater.* **2012**, *24*, 294–298.

[6] Li, X.; Yang, J. *Phys. Chem. Chem. Phys.* **2013**, *15*, 15793–15801.

[7] Li, X.; Wu, X.; Li, Z.; Yang, J.; Hou, J. G. *Nanoscale* **2012,** *4*(18), 5680-5685.

[8] Geim, A. K.; Novoselov, K. S. *Nat. Mater.* **2007**, *6*(3), 183-191.

[9] Novoselov, K. S.; Mishchenko, A.; Carvalho, A.; Neto, A. C. *Science* **2016**, *353*, 6298.

[10] Neto, A. C.; Guinea, F.; Peres, N. M. R.; Novoselov, K. S.; Geim, A. K. *Rev. Mod. Phys.* **2009**, *81*(1), 109.

[11] Liu, Y.; Weiss, N.O.; Duan, X.; Cheng, H. C.; Huang, Y.; Duan, X. *Nat. Rev. Mater.* **2016**, *1*, 16042.

[12] Wang, Z. F.; Liu, Z.; Liu, F. *Nat. Commun.* **2013**, *4*, 1471.

[13] Zhou, M.; Ming, W.; Liu, Z.; Wang, Z.; Li, P.; Liu, F. *Proc. Natl. Acad. Sci.* **2014**, *111*(40), 14378–14381.

[14] Zhou, M.; Liu, Z.; Ming, W.; Wang, Z.; Liu, F. *Phys. Rev. Lett.* **2014**, *113*(23), 236802.

[15] Dutta, S.; Pati, S. K. *J. Phys. Chem. B* **2008**, *112*(5), 1333–1335.

[16] Dutta, S.; Manna, A. K.; Pati, S. K. *Phys. Rev. Lett.* **2009**, *102*(9), 096601.

[17] Oeiras, R. Y.; Araujo-Moreira, F. M.; Da Silva, E. Z. *Phys. Rev. B* **2009**, *80*(7), 073405.

[18] Porter, C. D.; Stroud, D. *Phys. Rev. B* **2012**, *85*, 235452.

[19] Y. W. Son, M. L. Cohen and S. G. Louie, Nature 2006, 444, 347–349.

[20] Naguib, M.; Mashtalir, O.; Carle, J.; Presser, V.; Lu, J.; Hultman, L.; Barsoum, M. W. *ACS Nano* **2012**, *6*, 1322–1331.

[21] Naguib, M.; Mochalin, V. N.; Barsoum, M. W.; Gogotsi, Y. *Adv. Mater.* **2014**, *26*, 992–1005.

[22] Naguib, M.; Kurtoglu, M.; Presser, V.; Lu, J.; Niu, J.; Heon, M.; Barsoum, M. W. *Adv. Mater.* **2011**, *23*, 4248–4253.

[23] Si, C.; Zhou, J.; Sun, Z. *ACS Appl. Mater. Interfaces* **2015**, *7*, 17510–17515.

[24] Lane, N. J.; Barsoum, M. W.; Rondinelli, J. M. *EPL* **2013**, *101*(5), 57004

[25] Khazaei, M.; Arai, M.; Sasaki, T.; Chung, C. Y.; Venkataramanan, N. S.; Estili, M.; Kawazoe, Y. *Adv. Funct. Mater.* **2013**, *23*(17), 2185–2192.

[26] Gao, G.; Ding, G.; Li, J.; Yao, K.; Wu, M.; Qian, M. *Nanoscale* **2016**, *8*(16), 8986–8994.

[27] Hu, J.; Xu, B.; Ouyang, C.; Yang, S. A.; Yao, Y. *J. Phys. Chem. C* **2014**, *118*(42), 24274–24281.

[28] Xie, Y.; Kent, P. R. C. *Phys. Rev. B* **2013**, *87*, 235441.

[29] Lee, Y.; Cho, S. B.; Chung, Y. C. *ACS Appl. Mater. Interfaces* **2014**, *6*, 14724–14728.

[30] McGuire, M. A.; Dixit, H.; Cooper, V. R.; Sales, B. C. *Chem. Mater.* **2015**, *27*(2), 612–620.

[31] Hillebrecht, H.; Schmidt, P. J.; Rotter, H. W.; Thiele, G.; Zonnchen, P.; Bengel, H.; Whangbo, M. H. *J. Alloys Compd.* **1997**, *246*(1), 70–79.

[32] Zhang, W. B.; Qu, Q.; Zhu, P.; Lam, C. H. *J. Mater. Chem. C* **2015**, *3*(48), 12457–12468.

[33] Miro, P.; Audiffred, M.; Heine, T. *Chem. Soc. Rev.* **2014**, *43*(18), 6537–6554.

[34] Ziatdinov, M.; Arnab Banerjee, A.; Maksov, Berlijn, T.; Zhou, W.; Cao, H. B.; Yan, J-Q. *et al. Nat. Commun.* **2016**, *7*, 13774.

[35] Weber, D.; Schoop, L.M.; Duppel, V.; Lippmann, J.M.; Nuss, J.; Lotsch, B.V. *Nano Lett.* **2016**, *16*(6), 3578-3584.

[36] Huang, B.; Clark, G.; Navarro-Moratalla, E.; Klein, D.R.; Cheng, R.; Seyler, K.L.; Zhong, D.; Schmidgall, E.; McGuire, M.A.; Cobden, D.H.; Yao, W. *Nature* **2017**, *546*(7657), 270-273.

[37] McGuire, M.A.; Clark, G.; KC, S.; Chance, W.M.; Jellison Jr, G.E.; Cooper, V. R.; Xu, X.; Sales, B.C.;., *arXiv preprint arXiv:* **2017**, 1706.01796.

[38] Zhong, D.; Seyler, K. L.; Linpeng, X.; Cheng, R.; Sivadas, N.; Huang, B.; Schmidgall, E.; Taniguchi, T.; Watanabe, K.; McGuire, M.A.; Yao, W. *Sci. Adv.* **2017**, *3*(5), 1603113.

[39] Born, M.; Oppenheimer, R. *Annalen der Physik,* **1927,** *84*, 457.

[40] Hohenberg, P.; Kohn, W. *Phys. Rev.* **1964**, *136*, B864.

[41] Kohn, W.; Sham, L. J. *Phys. Rev.* **1965**, *140*, A1133.

[42] Perdew, J. P.; Zunger, A. *Phys. Rev. B* **1981**, *23*, 5048.

[43] Dirac, P. A. M. *Proc. Cambridge Phil. Roy. Soc.* **1930**, *26*, 376.

[44] Thomas, L. H. *Proc. Cambridge Phil. Roy. Soc.* **1927**, *23*, 542.

[45] Fermi, E. *Rend. Accad. Naz. Lincei* **1927**, 6, 602.

[46] Becke, A. D. *Phys. Rev. A* **1988**, *38*, 3098.

[47] Perdew, J. P., Chevary, J. A.; Vosko, S. H.; Jackson, K. A.; Pederson, M. R.; Fiolhais, C. *Phys. Rev. B* **1992**, *46*, 6671.

[48] Perdew, J. P.; Burke, K.; Ernzerhof, M. *Phys. Rev. Lett.* **1996**, 77, 3865.

[49] Stephens, P. J.; Devlin, F. J.; Chabalowski, C. F.; Frisch, M. J. *J. Phys. Chem.* **1994**, *98*(45),11623–11627.

[50] Lee, C.; Yang, W.; Parr, R.G. *Phys. Rev. B* **1988**, *37*(2), 785.

[51] Heyd, J.; Scuseria, G. E.; Ernzerhof, M. *J. Chem. Phys.* **2003**, *118*(18), 8207-8215.

[52] Adamo, C.; Barone, V. *J. Chem. Phys.* **1999**, *110*(13), 6158-6170.

[53] Anisimov, V. I.; Aryasetiawan, F.; Lichtenstein, A. I. *J. Phys. Condens. Matter.* **1997**, 9, 767.

[54] Dudarev, S. L.; Botton, G. A.; Savrasov, S. Y.; Humphreys, C. J.; Sutton, A. P. *Phys. Rev. B* **1998**, *57*, 1505.

[55] Cococcioni, M.; De Gironcoli, S. *Phys. Rev. B* **2005**, *71*, 035105.

[56] Hsu, H.; Blaha, P.; Cococcioni, M.; Wentzcovitch, R. M. *Phys. Rev. Lett.* **2011**, *106,* 118501 (2011)

[57] Gonze, X.; Allan, D. C.; Teter, M. P. *Phys. Rev. Lett.* **1992**, *68*, 3603 (1992)

[58] http://www.quantum-espresso.org/

[59] Parlinski, K.; Li, Z. Q.; Kawazoe, Y. *Phys. Rev. Lett.* **1997**, *78*, 4063.

[60] Togo, A.; Oba, F.; Tanaka, I. *Phys. Rev. B* **2008**, *78*(13), 134106.

[61] Savrasov, S. Y. *Phys. Rev. Lett.* **1992**, *69*, 2819.

[62] Kühne, T. D. *Com. Mol. Sci.* **2014**, *4*(4), 391-406.

[63] Kresse, G.; Joubert, D. *Phys. Rev. B* **1999**, *59*, 1758

[64] Griffith, J. S. *Theory of transition-metal ions; Cambridge University Press: New York*, **1961**

[65] He, J.; Jiao, N.; Zhang, C.; Xiao, H.; Chen, X.; Sun, L. *J. Phys. Chem. C* **2014**, *118*(17), 8899-8906.

[66] Wehling, T. O.; Lichtenstein, A. I.; Katsnelson, M. I. *Phys. Rev. B* **2011**, *84*, 235110

[67] Ali, M. E.; Sanyal, B.; Oppeneer, P. M. *J. Phys. Chem. B* **2012**, *116*, 5849-5859

[68] Xiang, H.; Lee, C.; Koo, H. J.; Gong, X.; Whangbo, M. H. Dalton Transactions **2013**, *42*(4), 823-853.

[69] Weiss, P. *J. de Phys.* **1907**, *6*, 661-690.

[70] Newman, M. E. J. ; Barkema, G. T. Monte Carlo Methods in Statistical Physics, Clarendon Press, **1999.**

[71] Hay, P. J.; Thibeault, J. C.; Hoffmann, R. *J. Am. Chem. Soc.* **1975**, *97*, 4884.

[72] He, J.; Zhou, P.; Jiao, N.; Ma, S. Y.; Zhang, K. W.; Wang, R. Z.; Sun, L. Z. *Sci. Rep.* **2014**, *4*, 4014.

[73] Wang, X.; Shen, X.; Gao, Y.; Wang, Z.; Yu, R.; Chen, L. *J. Am.n Chem. Soc.* **2015**, *137*(7), 2715-2721.

[74] Hope, M. A.; Forse, A. C.; Griffith, K. J.; Lukatskaya, M. R.; Ghidiu, M.; Gogotsi, Y.; Grey, C. P. *Phys. Chem. Chem. Phys.* **2016**, *18*, 5099.

[75] Ingason, A. S.; Petruhins, A.; Dahlqvist, M.; Magnus, F.; Mockute, A.; Alling, B.; Rosen, J. *Mater. Res. Lett.* **2014**, *2*(2), 89-93.

[76] Thore, A.; Dahlqvist, M.; Alling, B.; Rosén, J. *Phys. Rev. B* **2016**, *93*(5), 054432.

[77] Thore, A.; Dahlqvist, M.; Alling, B.; Rosén, J. *J. Appl. Phys.* **2014**, *116*(1s0), 103511.

[78] Dahlqvist, M.; Ingason, A. S.; Alling, B.; Magnus, F.; Thore, A.; Petruhins, A.; Abrikosov, I. A. *Phys. Rev. B* **2016**, *93*(1), 014410.

[79] Li, X.; Yang, J. *J. Mater. Chem. C* **2014**, *2*(34), 7071-7076.

[80] Kobayashi, K. I.; Kimura, T.; Sawada, H. *et al. Nature* **1998**, *395*(6703), 677-680.

[81] Xie, W. H.; Xu, Y. Q.; Liu, B. G. *et al. Phys. Rev. Lett.* **2003**, *91*(3), 037204.

[82] Hu, L.; Wu, X.; Yang, J. *Nanoscale* **2016**, *8*, 12939-12945.

[83] Daalderop, G. H. O., Kelly, P. J.; Schuurmans, M. F. H. *Phys. Rev. B* **1990**, *41*(17), 11919.

[84] Chang, C. Z.; Zhang, J.; Feng, X.; Shen, J.; Zhang, Z.; Guo, M.; Ji, Z. Q. *Science* **2013**, *340*, 167-170.

[85] Lee, C.; Wei, X.; Kysar, J. W.; Hone, J. *Science* **2008**, *321*, 385–388.

[86] Cahangirov, S.; Topsakal, M.; Aktürk, E.; Şahin, H.; Ciraci, S. *Phys. Rev. Lett.* **2009**, *102*(23), 236804.

[87] Şahin, H.; Cahangirov, S.; Topsakal, M.; Bekaroglu, E.; Akturk, E.; Senger, R.T.; Ciraci, S. *Phys. Rev. B* **2009**, *80*(15), 155453.

[88] Mostofi, A.; Yates, J. R.; Lee, Y. S.; Souza, I.; Vanderbilt D.; Marzari, N. *Comput. Phys. Commun.* **2008**, *178*, 685.

[89] Sancho, M. L.; Sancho, J. L.; Rubio, J. *J. Phys. F: Met. Phys.* **1984**, *14*, 1205

List of Attached Publications

This thesis is based on the following articles

Attachment A:

Reprinted with permission from **Junjie He**, Pengbo Lyu, Lizhong Sun, Angel Morales-Garcia, Petr Nachtigall, *Two-dimensional Janus MXenes: High-temperature Spin-polarized Semiconductor with Zero Magnetization*. ***Journal of Materials Chemistry C***, 4, 6500-6509, 2016. Copyright (2016) Royal Society of Chemistry. To download this article, please use

http://pubs.rsc.org/-/content/articlelanding/2016/tc/c6tc01287f#!divAbstract

Attachment B:

Reprinted with permission from **Junjie He**, Pengbo Lyu, Petr Nachtigall, *New Two-Dimensional Mn-based MXenes with Room-Temperature Ferromagnetism and Half-Metallicity.* ***Journal of Materials Chemistry C***, 4, 11143-11149, 2016. Copyright (2016) Royal Society of Chemistry. To download this article, please use

http://pubs.rsc.org/-/content/articlelanding/2016/tc/c6tc03917k#!divAbstract

Attachment C:

Reprinted with permission from **Junjie He**, ShuangYing Ma, Pengbo Lyu, Petr Nachtigall, *Unusual Dirac Half-Metallicity with Intrinsic Ferromagnetism in Vanadium Trihalides Monolayers*. ***Journal of Materials Chemistry C***, 4(13), 2518-2526, 2016. Copyright (2016) Royal Society of Chemistry. To download this article, please use

http://pubs.rsc.org/-/content/articlelanding/2016/tc/c6tc00409a#!divAbstract

Attachment D:

Attached Publications